Title: Eco-evolutionary significance of 'loners'

Authors: Fernando W. Rossine[1,§], Ricardo Martinez-Garcia[1,§], Allyson E. Sgro[2,†], Thomas Gregor[2,*], Corina E. Tarnita[1,*]

Affiliations: [1] Department of Ecology and Evolutionary Biology, Princeton University, Princeton NJ 08544, USA
[2] Joseph Henry Laboratories of Physics and Lewis-Sigler Institute for Integrative Genomics, Princeton University, Princeton, NJ 08544, USA

[§] Equal contribution
[*] Corresponding author
[†] Current address: Department of Biomedical Engineering and the Biological Design Center, Boston University, Boston, MA 02215

Abstract: Loners, individuals out-of-sync with a coordinated majority, occur frequently in nature. Are loners incidental byproducts of large-scale synchronization attempts or are they part of a mosaic of life-history strategies? Here, we provide the first empirical evidence of naturally occurring heritable variation in loner behavior, using the social amoeba *Dictyostelium discoideum*. Moreover, we show that *Dictyostelium* loners—cells that do not join the multicellular life-stage— result from a dynamic population-partitioning process. Underlying this partitioning, we find evidence that each cell makes a stochastic, signal-based decision resulting in an imperfectly synchronized multicellular development affected by both abiotic (environmental porosity) and biotic (strain-specific signaling) factors. Finally, we predict that when strains differing in their partitioning behavior co-occur, cross-signaling impacts slime-mold diversity across spatio-temporal scales. Loners are therefore critical to understanding collective and social behaviors, multicellular development, and ecological dynamics in *D. discoideum*. More broadly, across taxa, imperfect synchronization might be adaptive by enabling diversification of life-history strategies.

Introduction

Collective behaviors, in which a large number of individuals exhibit some degree of behavioral synchronization, are frequent across the tree of life and across spatio-temporal scales: from microbial aggregates to the great wildebeest migration, from locust swarming to synchronized bamboo flowering, from fish schooling to mechanical adaptation in honeybee clusters (Couzin & Krause, 2003; Gregor, Fujimoto, Masaki, & Sawai, 2010; Hopcraft et al., 2015; Janzen, 1976; Kaiser & Crosby, 1983; Katz, Tunstrom, Ioannou, Huepe, & Couzin, 2011; Peleg, Peters, Salcedo, & Mahadevan, 2018; Simpson, McCaffery, & Hägele, 1999). Intriguingly, however, such synchronization is sometimes imperfect and 'out-of-sync' individuals (henceforth loners), have been reported in several of these systems. For instance, in locusts, population crowding prompts a transition from a solitary phase, in which individuals repel each other, to a gregarious phase, in which they attract each other. Experiments show, however, that not all individuals undergo this transition, even if exposed to long periods of crowding (Simpson et al., 1999). In wildebeest, hundreds of thousands of individuals coordinate with each other and organize herding migrations, but resident populations, that fail to migrate, also exist (Hopcraft et al., 2015). Similarly, wildebeest calving times are also highly coordinated, but some fraction of the calves are born outside the calving period (Hopcraft et al., 2015). In bamboo, individuals predominantly flower in synchronized masts, but sporadic out-of-sync events have also been recorded (Janzen, 1976).

The roots of imperfect synchronization will undoubtedly differ across systems. Nevertheless, the occurrence of imperfect synchronization across such different systems and scales raises fundamental questions about its causes and consequences. Are loners mistakes—merely inevitable byproducts of large scale synchronization attempts—or are they a variable trait that selection can shape with potential ecological consequences? Theoretical investigations of such loner behaviors have been sparse, but the handful of existing studies have suggested that, at least in some systems, they could be a means of spatio-temporal niche-partitioning (Dubravcic, van Baalen, & Nizak, 2014) that promotes diversity (Martínez-García & Tarnita, 2017; Tarnita, Washburne, Martínez-García, Sgro, & Levin, 2015). However, despite this theoretically established potential, variability and heritability of loner behaviors have not been characterized in natural populations. Thus, there exists no empirical evidence, in any system, that loners are anything more than chance stragglers, lacking an avenue for selection to act on them.

The cellular slime mold *Dictyostelium discoideum* is an ideal system in which to experimentally characterize loner behaviors. Its life cycle comprises a unicellular feeding stage and a starvation-induced multicellular stage—the result of a developmental process involving coordinated cell aggregation, which culminates in the production of starvation-resistant spores (Bonner, 2009). There has been extensive progress in understanding this multicellular stage (Bonner, 2009; Gregor et al., 2010; Strassmann & Queller, 2011), but less attention has been paid to the potential role of asocial aspects—such as the non-aggregating solitary loner-cells—in development. Loners die under sustained starvation, but they persist temporarily (Dubravcic, 2013); if food is replenished, they eat and divide, and their progeny subsequently recapitulate the multicellular development (Tarnita et al., 2015). Finally, it has been shown that knockout strains can have different loner behaviors (Dubravcic et al., 2014). Altogether, these observations suggest that loners could indeed be part of a life-history strategy in *D. discoideum*. However, to fully establish this, one needs to show (a) that there are evolutionary paths such that loner behavior can be tuned while populations retain viability in their natural environments and (b) that there are fitness differences between strains with different loner behaviors in natural environments. Here we tackle (a) by inspecting

2

78   loner behavior in naturally occurring strains; in the process, we uncover the cellular decision-
79   making rules underlying the aggregator-loner partitioning and explore their potential ecological
80   consequences.

Results and Discussion

81

The aggregator-loner partitioning is heritable and context-dependent

82

83   To determine whether the loner behavior is heritable—and, thus, whether there is the potential for
84   natural selection to act on it—we developed an experimental protocol to identify individual loner
85   cells (Fig. 1a,b), permitting us to characterize their spatial distribution (Fig. 1c, Fig. S1) and
86   quantify their density (Fig. 1d,e, Fig. S2). Importantly, we worked with three natural isolates (i.e.
87   strains or genetic variants) that were collected from the same location to ensure that observed
88   behaviors of individual strains were not an artifact of lab rearing and that observed behavioral
89   differences among strains reflected naturally co-occurring strategies. When homogeneously plated
90   cells of a given strain were left to starve and undergo multicellular development, loner cells were
91   found throughout aggregation territories, with a higher density at territory borders and at
92   experimental boundary conditions than in the immediate surroundings of aggregation centers (Fig
93   1c, Fig. S1). In repeated experiments under controlled conditions, loner densities of a given strain
94   fell consistently within a conserved distribution (framed portion of Fig. 1e); moreover, the loner
95   distributions of some strains were significantly different in their mean and variance (compare
96   strains NC28.1 and NC85.2 in Fig. 1d, and framed portion of Fig. 1e). These findings demonstrate
97   that the aggregator-loner partitioning behavior is heritable and thus has the potential to be shaped
98   by selection.

99   To characterize the underlying developmental process, it must first be determined whether a cell's
100   decision to commit to aggregation or remain a loner is context-independent (Dubravcic et al., 2014;
101   Tarnita et al., 2015) (the result of a stochastic switch) or whether it depends on external factors. If
102   it is context-independent, then loner density should increase linearly with the density of initially
103   plated cells, i.e., the heritable quantity would be the fraction of loners, as previously posited
104   (Dubravcic et al., 2014; Tarnita et al., 2015). Instead, we found a non-linear dependence: at low
105   initial densities, cells were too sparse for aggregation to occur and all cells remained loners; above
106   a threshold, aggregation occurred with increasing efficiency and loner densities decreased;
107   surprisingly, at high initial cell densities, loner densities plateaued (Fig. 1d, Fig. S2c-k). Thus, past
108   a range of initial densities, it is the *number* (or density), and not the *fraction,* of loners that is
109   heritable, suggesting an underlying cell decision-making process that is fundamentally different
110   from a stochastic switch. Furthermore, when we varied the porosity of the agar substrate—a proxy
111   for an important environmental characteristic for this soil-dwelling amoeba—less porous (more
112   concentrated) agar yielded higher loner densities (Fig. 1e), and differentially affected *D.*
113   *discoideum* strains by enhancing the difference between strains that leave fewer loners ('better
114   aggregators') and those that leave more loners ('worse aggregators'). Interestingly, the agar
115   porosity affects not only the mean number of loners, but also the variance (Fig. 1e). Altogether,
116   these findings demonstrate that the heritable aggregator-loner partitioning is context-dependent—
117   the result of a density-dependent decision-making process (Balázsi, Van Oudenaarden, & Collins,
118   2011) that interacts with the abiotic environment.

119   **The aggregator-loner partitioning is the result of an abiotically-modulated quorum-based**
120   **stochastic process.**

3

121 To identify the properties of this decision-making process, we constructed a spatially explicit
122 individual-based model (Fig. S3; see Methods) starting from a limited set of assumptions: that the
123 strain-specific partitioning behavior results from imperfect synchronization in the developmental
124 program, and that this asynchrony stems from a stochastic response to cell-population densities
125 (i.e., quorum sensing). Consistent with our experimental design, we started with a population of
126 cells immediately after food exhaustion and assumed them to be in a pre-aggregating state, *P*. *P*-
127 cells emit extracellular signaling molecules at a strain-specific rate γ; signal diffuses with diffusion
128 coefficient *D* and serves a quorum-sensing purpose (Gregor et al., 2010; Loomis, 2014) that
129 regulates the stochastic transition to the aggregating state, *A*: when the signal perceived by a cell
130 exceeds the strain-specific sensitivity threshold θ (i.e. the quorum is met), that cell has a strain-
131 specific probability λ per unit time of becoming an aggregating *A*-cell. *A*-cells continue to emit
132 signal and move towards the aggregation center with constant, strain-specific velocity v. At the
133 center, cells become multicellular (*M*-state) and stop emitting signal. Importantly, we do not
134 impose restrictions on the nature of the signaling molecule or on the sensing mechanism, and the
135 model employs this molecule broadly to fulfill both a traditional (Gomer, Yuen, & Firtel, 1991;
136 Loomis, 2014) and a dynamical quorum sensing role (Gregor et al., 2010).

137 Because our model is focused on population partitioning, it deliberately simplifies certain
138 dynamics (Dallon & Othmer, 1997; Gregor et al., 2010; Keller & Segel, 1970; Kessler & Levine,
139 1993; Palsson & Othmer, 2000; Sawai, Thomason, & Cox, 2005) and it bundles many possible
140 intermediate states that make up the *P*-to-*A* transition: for example, before aggregating, cells must
141 sequentially starve, become excitable by cAMP (Clarke & Gomer, 1995; Jain, Yuen, Taphouse, &
142 Gomer, 1992), and finally chemotax (Gregor et al., 2010). Moreover, for computational
143 convenience, our model simplifies various sources of stochasticity that arise during the
144 developmental process, such as the existence of multiple aggregation territories and the variable
145 boundary shapes between them. This prevents us from studying the sources and dynamics of the
146 variance in loner density, an important direction for future work. Nevertheless, this reduced model
147 is powerful enough to qualitatively recapitulate all other properties of the observed population
148 partitioning (Fig. 1f; Fig. S4a-e). Importantly, the model recovers the plateau in the loner counts
149 as a function of initially-plated cell density (Fig. 1f; Fig. S4a-d; Box 1 and SI Appendix) and it
150 provides an intuition for the identity of the loners (Fig. 2): they are *P*-cells that did not make the
151 probabilistic transition to the *A*-state when they had a quorum and that are left without a quorum
152 when enough of their neighbors underwent the *P*-to-*A* transition and moved towards the
153 aggregation center.

154 Total loner density then depends on how quickly *P*-cells switch to the *A*-state relative to how
155 quickly they are left without a quorum (λ/v), and on how easy it is to maintain a quorum (see Fig.
156 S4a-d, Box 1 and SI Appendix for analytical results). Thus, the larger the *P*-to-*A* transition rate λ,
157 the fewer loner cells are left behind since *P*-cells sensing a quorum switch faster to the *A*-state;
158 conversely, the larger the aggregation speed v, the more loners are left behind since *A*-cells move
159 away faster and leave their *P*-cell neighbors without a quorum (Fig. S4c). Consequently, the farther
160 a cell is from the aggregation center, the sooner it is left without a quorum and the more likely it
161 is to become a loner (Fig. S4e), which explains our experimentally observed spatial distribution
162 (Fig. 1c).

163 Achieving and maintaining a quorum depends on the ratio between the sensitivity threshold and
164 the signaling rate, $\kappa = \theta/\gamma$, and on the signal diffusivity, *D*. Higher κ leads to more loners because
165 more neighbors are required for a quorum (Fig. S4d). Similarly, lower diffusivities result in higher

4

166 loner densities (Fig. S4f,g) because the signal remains highly concentrated around the emitters,
167 and cells need to be more densely packed to maintain a quorum (Fig. S4h,i). Moreover, decreasing
168 the diffusivity differentially affects worse and better aggregators (Fig. 1g, Fig. S4f,g), because
169 diffusivity and signal spreading are nonlinearly related (see Methods). These results mirror the
170 experimentally determined dependence of loner densities on agar concentration, suggesting signal
171 diffusivity as a potential mediator of this dependency. Because loner densities responded to agar-
172 concentration changes in a range that should not impede the diffusion of cAMP (Johnson, Berk,
173 Jain, & Deen, 1996; Pluen, Netti, Jain, & Berk, 1999), these results further suggest that at least
174 one of the molecules involved in the quorum-dependent transition should be large—for example,
175 conditioned medium factor (CMF)(Gomer et al., 1991), prestarvation factor (PSF) counting factor
176 (Kolbinger et al., 2005), counting factor (Brock & Gomer, 1999) or phosphodiesterase
177 (Bodenschatz, Bae, & Prabhakara, 2017).

178 Notably, PSF and CMF are secreted during the growth phase and early starvation. This led us to
179 investigate the potential role that these earlier signaling stages could play in regulating loner
180 behavior. To test this hypothesis, we let cells grow in bacterial suspension until resources are
181 depleted, and only subsequently plated them in agar gels. Thus, the initial responses to resource
182 depletion occur in a well-mixed environment, and any signaling molecules secreted in this phase
183 should synchronously reach all cells. If early signaling is responsible both for the loner differences
184 between strains and for the effects of agar concentration on loners, we predicted that the well-
185 mixed environment should produce the same effects as increasing diffusion in our model (Fig 1g).
186 First, the increased signaling synchrony should decrease the loner number of any given strain;
187 second, strains that had more synchronous signaling to begin with (i.e. better aggregators) should
188 be less affected by this treatment than strains that started out with less synchronous signaling (i.e.
189 worse aggregators), which would cause the differences between strains to decrease. Consistent
190 with these predictions, we found that the loner counts decreased dramatically for the worse
191 aggregator, leading to a reduction in the difference between strains (Fig. 3). This supports our
192 hypothesis that vegetative or early starvation signaling—and not the later, cAMP relay signaling
193 and synchronization, as previously inferred using knockouts (Dubravcic et al., 2014)—could be a
194 critical stage at which loner behavior is regulated and the natural variation that we observed is
195 produced.

The aggregator-loner partitioning depends on the identity of neighboring cells.
197 Collectively, the results above show that the population partitioning stems from interactions
198 between genotype and environment and suggest that cell signaling mediates these interactions.
199 This raises the possibility that a strain's partitioning could also be influenced by the presence of
200 other strains via cross-signalling. If a cell's commitment to aggregation were independent of the
201 identity of co-occurring strains, a mix of strains would leave behind a total mixed loner density
202 that is the linear combination of the two strains' loner densities (see Methods). Our model,
203 however, predicts developmental interactions between co-occurring strains that produce a diversity
204 of departures from linearity (Fig. 4a; Fig. S5).

205 When we plated well-mixed cells of the strains NC28.1 (better aggregator) and NC85.2 (worse
206 aggregator) at different frequencies and left them to co-develop under starvation conditions we
207 found agreement with this theoretical prediction. The total loner density of the mixed strains
208 deviated significantly from the linear combination, mapping out a sigmoidal curve (Fig. 4b, Fig.
209 S6), which was one of three possible theoretical outcomes. Thus, when the better aggregator was
210 more abundant in the mix (25%:75%) there were fewer total loners than predicted by the linear

211 combination; conversely, when the worse aggregator was more abundant (75%:25%) there were
212 more total loners. That strains influence each other's partitioning is consistent with existing results
213 using knockouts (Dubravcic et al., 2014) and it is particularly interesting in light of prior work
214 showing that, during aggregation, *D. discoideum* cells do not perfectly discriminate against non-
215 kin and genetically heterogeneous multicellular aggregates occur naturally (Strassmann, Zhu, &
216 Queller, 2000), allowing for potential interactions between strains that can alter each other's life-
217 history investments (Buttery, Rozen, Wolf, & Thompson, 2009; Strassmann & Queller, 2011).
218 Whether or not such interactions occur within the aggregate (Martínez-García & Tarnita, 2016;
219 Tarnita et al., 2015; J. B. B. Wolf et al., 2015), our results reveal that they do occur earlier in the
220 developmental process.

221 Such developmental interactions that alter life history investments could severely impact strain
222 fitness, alter *D. discoideum* diversity, and threaten the persistence of the social behavior
223 (Strassmann & Queller, 2011). It is therefore crucial to understand their consequences for
224 individual strains. In our case, the theoretical model produced two possible outcomes of co-
225 development (see SI Appendix): the two co-occurring strains can become either (i) more similar
226 (Fig. S7a,b) or (ii) more different (Fig. S7c,d) in their partitioning behavior. In particular, when
227 the theoretical density of the mixed-strain loners had a sigmoidal shape similar to that derived
228 experimentally, the loners of the better aggregator quickly went to zero as the frequency of the
229 worse aggregator in the mix increased (Fig. S7c,d). Thus, the better aggregator became even better
230 in the presence of the worse aggregator, enhancing the difference between the two strains (case ii).
231 This occurred because the more sluggish loners of the worse aggregator maintained quorum long
232 enough for the better aggregator to aggregate perfectly. Experimentally, the spatial distribution of
233 the mixed-strain loners provides insight into their potential composition (Fig. 4c,d): as soon as the
234 worse aggregator is part of the mix (even at the lowest frequency), the spatial distribution of the
235 mixed loners is almost identical to that of the worse aggregator—and strikingly different from that
236 of the better aggregator—suggesting that, as predicted, the mixed-strain loners predominantly
237 comprise the worse aggregator. Importantly, developmental interactions between co-occurring
238 strains do indeed have consequences for the life history investments of individual strains.

Cross-signaling may foster slime mold diversity across spatio-temporal scales.
240 The two possible outcomes of co-development predicted by our population-partitioning model are
241 reminiscent of two classical evolutionary routes to diversity maintenance—quasi-neutrality (case
242 i; Fig. 5a) and character displacement (case ii; Fig. 5b)—and are therefore likely to have
243 consequences for slime-mold diversity. To investigate these biodiversity consequences of strains
244 mixing and co-developing—instead of perfectly segregating and avoiding co-development—we
245 incorporated our population-partitioning model into an existing model of competition for resources
246 over multiple successive growth-starvation (Martínez-García & Tarnita, 2016, 2017; Tarnita et al.,
247 2015) (Fig. S8; see Methods). Although empirically we did not investigate fitness differences
248 between strains, here we assume that such differences exist and depend on the environmental
249 conditions as in prior work (Martínez-García & Tarnita, 2016, 2017; Tarnita et al., 2015). The
250 environment is characterized by the mean time between nutrient replenishment events. We
251 considered both deterministic environments (all replenishment times of equal size) and stochastic
252 environments (exponentially distributed nutrient replenishment times). For each, we explored a
253 range of mean nutrient replenishment times. Regardless of whether co-development occurs, within
254 any environment, there was competitive exclusion: consistent with previous work, we found that
255 strains that leave behind more (fewer) loners are more competitive in environments with shorter

256 (longer) mean replenishment times (Tarnita et al., 2015). In deterministic environments the identity
257 of the winner was also deterministic and not altered by co-development (inset of Fig. 5c,d);
258 however, co-development did alter the time-to-extinction of the loser (inset of Fig. 5e,f). On the
259 contrary, in stochastic environments, for every pair of competing strains, there is a range of
260 environments where the identity of the winner is uncertain and that range is drastically altered by
261 co-development (Fig. 5c,d). As in deterministic environments, co-development also influenced the
262 time-to-extinction of the loser (Fig. 5e,f).

263 To untangle the effects of co-development on diversity at different spatial scales, we discretized
264 the environment into small-scale patches with identical replenishment conditions. Competition
265 between pairs of strains occurred within each patch, and there was no dispersal between patches.
266 Importantly, this setup allows us to investigate the effects of co-development on alpha (intra-patch)
267 and beta (inter-patch) diversity, but it does not introduce any intrinsic spatial heterogeneity. As
268 expected, within each patch, we found competitive exclusion. However, at the level of the
269 environment, if the replenishment conditions are within the range where the identity of the winner
270 is uncertain, there can be coexistence. Each of our predicted modes of co-development imparted a
271 distinct biodiversity signature. Specifically, in case (i), the converging behaviors of the two strains
272 led to much longer times to extinction, resulting in higher transient alpha diversity compared to
273 the segregated model. However, this mode of co-development also narrowed the environmental
274 range in which competition lead to non-deterministic exclusion, resulting in lower stationary beta
275 diversity compared to the segregated model (Fig. 6a). Case (ii) yielded the opposite outcome for
276 both alpha and beta diversity (Fig. 6b).

Conclusion

278 To conclude, here we showed natural variation and heritability in the aggregator-loner partitioning
279 behavior of naturally co-occurring strains of *D. discoideum*. Strikingly, the seemingly asocial
280 loners are not a separate, independently-determined subset of cells, but rather they arise
281 dynamically from the collective process. Coupling experiments and theory, we revealed that the
282 aggregator-loner partitioning behavior is governed by a stochastic cell-level decision-making
283 process mediated by cell signaling and modulated by both the abiotic and the biotic context. These
284 investigations of collective behavior revealed previously unknown stochastic aspects of *D.
285 discoideum* development. Finally, we used a theoretical approach to explore the ecological
286 consequences of these findings and showed that the co-development of different strains impacts
287 diversity across multiple scales. These results, arising solely from interactions between ecology
288 and development, recapitulate the biodiversity outcomes of classical eco-evolutionary interactions.
289 Overall, our results highlight the necessity of an integrated approach to collective behaviors,
290 including multicellularity: studying asocial life-history strategies revealed insights into collective
291 behavior and development, and studying development revealed insights into ecological dynamics
292 and parallels with well-studied eco-evolutionary processes.

293 Furthermore, our findings have potentially fundamental implications for the evolution of
294 aggregative multicellularity and social behaviors. Many factors could undermine the integrity of
295 social complexes, such as free-riding, whereby individuals reap the benefits of group living
296 without paying the costs. In slime molds, free-riders—strains that never contribute to stalk
297 formation in mixes—have been found both in the wild (Buss, 1982) and in the lab (Kuzdzal-Fick,
298 Fox, Strassmann, & Queller, 2011). If under selection, the heritable loners, invulnerable to the
299 threats to the multicellular stage but capable of re-achieving multicellularity via their offspring,

300 could constitute insurance against such threats and could therefore be critical to the evolution and
301 persistence of aggregative multicellularity. This hypothesis is consistent with the handful of
302 theoretical studies on cooperative behaviors that have considered social loners (Garcia, Doulcier,
303 & De Monte, 2015; Hauert, De Monte, Hofbauer, & Sigmund, 2002).
304
305 Finally, beyond multicellularity and sociality, our results have potential implications for the
306 broadly analogous loner behaviors identified across a variety of systems in which some form of
307 coordination or synchronization is observed, from insects (Simpson et al., 1999) to vertebrates
308 (Couzin & Krause, 2003; Hopcraft et al., 2015) to plants (Janzen, 1976). Our findings represent
309 the first demonstration that loner behaviors can indeed exhibit natural variation and heritability—
310 and that this can have significant ecological consequences—and, as such, they motivate a broader
311 investigation into loner behaviors in other systems. While the mechanisms underlying the
312 existence of loners are likely different across systems, the widespread existence of loners and the
313 possibility that they could in fact be shaped by selection suggest an interesting conjecture: that, in
314 general, imperfect synchronization may enable evolution to shape population-partitioning
315 strategies in ways that could be instrumental for behavioral diversity and for the persistence of the
316 collective stage, and thus for system-level robustness.
317

318
319 **Box 1**
320
321 In the spatially implicit limit ($D \longrightarrow \infty$, v finite) and in the limit of large initial population size
322 ($N_0 \longrightarrow \infty$), the density of loners ρ_L can be calculated analytically, which reveals the interactions
323 among model parameters (see SI Appendix). We find
324

$$\rho_L \propto \begin{cases} \kappa \left(1 - \dfrac{\lambda}{\tilde{v}} \right), & \text{if } \lambda < \tilde{v} \\ \qquad 0 \,, & \text{otherwise} \end{cases}$$

326
327 where $\kappa = \theta/\gamma$ is the ratio between the sensitivity threshold and the signaling rate, and $\tilde{v}$ is the
328 velocity rescaled by the mean distance traveled by cells before joining the aggregate. This reveals
329 a phase separation determined by the relative speeds of the two transitions, *P*-to-*A* and *A*-to-*M*
330 (Fig. S4b): a lack of synchronization resulting in loners occurs only if the *P*-to-*A* transition is
331 slower than the *A*-to-*M* transition.
332

---

333 # References

334 Balázsi, G., Van Oudenaarden, A., & Collins, J. J. (2011). Cellular decision making and biological
335   noise: From microbes to mammals. *Cell*, *144*(6), 910–925.
336   https://doi.org/10.1016/j.cell.2011.01.030
337 Bodenschatz, E., Bae, A. J., & Prabhakara, K. H. (2017). The cooperation of the haves and the
338   have-nots. *BioRxiv*, 234849. https://doi.org/10.1101/234849
339 Bonner, J. T. (2009). *The social amoebae: the biology of cellular slime molds*. Princeton University
340   Press.
341 Brock, D. A., & Gomer, R. H. (1999). A cell-counting factor regulating structure size in
342   *Dictyostelium*. *Genes and Development*, *13*(15), 1960–1969.

343   https://doi.org/10.1101/gad.13.15.1960

344 Buss, L. W. (1982). Somatic cell parasitism and the evolution of somatic tissue compatibility.
345   *Proceedings of the National Academy of Sciences of the United States of America*,
346   *79*(September), 5337–5341. https://doi.org/10.1073/pnas.79.17.5337

347 Buttery, N. J., Rozen, D. E., Wolf, J. B. B., & Thompson, C. R. L. (2009). Quantification of social
348   behavior in *Dictyostelium discoideum* reveals complex fixed and facultative strategies.
349   *Current Biology*, *19*(16), 1373–1377. https://doi.org/10.1016/j.cub.2009.06.058

350 Clarke, M., & Gomer, R. H. (1995, December). PSF and CMF, autocrine factors that regulate gene
351   expression during growth and early development of *Dictyostelium*. *Experientia*. Birkhäuser-
352   Verlag. https://doi.org/10.1007/BF01944730

353 Cotter, D. A., & Raper, K. B. (1968). Factors affecting the rate of heat-induced spore germination
354   in *Dictyostelium discoideum*. *Journal of Bacteriology*, *96*(1), 86–92. Retrieved from
355   http://www.ncbi.nlm.nih.gov/pubmed/4874316

356 Couzin, I. D., & Krause, J. (2003). Self-Organization and collective behavior in vertebrates. In
357   *Advances in the Study of Behavior* (Vol. 32, pp. 1–75). https://doi.org/10.1016/S0065-
358   3454(03)01001-5

359 D'Alessandro, J., Anjard, C., Mas, L., Aubry, L., Rieu, J.-P., & Rivière, C. (2018). Collective
360   regulation of cell motility using an accurate density-sensing system. *Journal Royal Society*
361   *Interface*, *15*, 20180006. Retrieved from http://dx.doi.org/10.1098/rsif.2018.0006

362 Dallon, J. C., & Othmer, H. (1997). A discrete cell model with adaptive signalling for aggregation
363   of *Dictyostelium discoideum*. *Philosophical Transactions of the Royal Society of London.*
364   *Series B, Biological Sciences*, *352*(1351), 391–417. https://doi.org/10.1098/rstb.1997.0029

365 Dubravcic, D. (2013). *Quantitative evolutionary analysis of the life cycle of social amoebae*.
366   Universite Rene Descartes - Paris V.

367 Dubravcic, D., van Baalen, M., & Nizak, C. (2014). An evolutionarily significant unicellular
368   strategy in response to starvation stress in *Dictyostelium* social amoebae. *F1000Research*,
369   *3*(133), 1–24. https://doi.org/10.12688/f1000research.4218.1

370 Dworkin, M., & Keller, K. H. (1977). Solubility and diffusion coefficient of adenosine 3': 5'-
371   monophosphate. *Journal of Biological Chemistry*, *252*(3), 864–865.

372 Fey, P., Dodson, R. J., Basu, S., & Chisholm, R. L. (2013). One stop shop for everything
373   *Dictyostelium*: DictyBase and the Dicty Stock Center in 2012. *Methods in Molecular Biology*,
374   *983*, 59–92. https://doi.org/10.1007/978-1-62703-302-2-4

375 Fey, P., Kowal, A. S., Gaudet, P., Pilcher, K. E., & Chisholm, R. L. (2007). Protocols for growth
376   and development of *Dictyostelium discoideum*. *Nature Protocols*, *2*(6), 1307–1316.
377   https://doi.org/10.1038/nprot.2007.178

378 Fisher, P. R., Merkl, R., & Gerisch, G. (1989). Quantitative analysis of cell motility and
379   chemotaxis in *Dictyostelium discoideum* by using an image processing system and a novel
380   chemotaxis chamber providing stationary chemical gradients. *The Journal of Cell Biology*,
381   *108*(3), 973–984. https://doi.org/10.1083/jcb.108.3.973

382 Francis, D., & Eisenberg, R. (1993). Genetic structure of a natural population of *Dictyostelium*
383   *discoideum*, a cellular slime mould. *Molecular Ecology*, *2*(6), 385–391.
384   https://doi.org/10.1111/j.1365-294X.1993.tb00031.x

385 Garcia, T., Doulcier, G., & De Monte, S. (2015). The evolution of adhesiveness as a social
386   adaptation. *ELife*, *4*, e08595. https://doi.org/10.7554/eLife.08595

387 Gomer, R. H., Yuen, I. S., & Firtel, R. A. (1991). A secreted 80x10(3)mr protein mediates sensing
388   of cell-density and the onset of development in *Dictyostelium*. *Development*, *112*(1), 269–

389   278.

390   Gregor, T., Fujimoto, K., Masaki, N., & Sawai, S. (2010). The onset of collective behavior in
391   social amoebae. *Science*, *328*(5981), 1021–1025. https://doi.org/10.1126/science.1183415

392   Hauert, C., De Monte, S., Hofbauer, J., & Sigmund, K. (2002). Volunteering as red queen
393   mechanism for cooperation in public goods games. *Science*, *296*(5570), 1129–1132.

394   Hopcraft, J. G. C., Holdo, R. M., Mwangomo, E., Mduma, S. A. R., Thirgood, S. J., Olff, H., &
395   Sinclair, A. R. E. (2015). Why are wildebeest the most abundant herbivore in the Serengeti
396   ecosystem? In F. J. Sinclair ARE, Metzger K, Mduma SAR (Ed.), *Serengeti IV: Sustaining*
397   *Biodiversity in a Coupled Human-Natural System*. Chicago: The University of Chicago Press.

398   Jain, R., Yuen, I. S., Taphouse, C. R., & Gomer, R. H. (1992). A density-sensing factor controls
399   development in *Dictyostelium*. *Genes and Development*, *6*(3), 390–400.
400   https://doi.org/10.1101/gad.6.3.390

401   Janzen, D. H. (1976). Why bamboos wait so long to flower. *Annual Review of Ecology and*
402   *Systematics*, *7*(1), 347–391. https://doi.org/10.1146/annurev.es.07.110176.002023

403   Johnson, E. M., Berk, D. A., Jain, R. K., & Deen, W. M. (1996). Hindered diffusion in agarose
404   gels: test of effective medium model. *Biophysical Journal*, *70*(2 I), 1017–1023.
405   https://doi.org/10.1016/S0006-3495(96)79645-5

406   Kaiser, D., & Crosby, C. (1983). Cell movement and its coordination in swarms of *Myxococcus*
407   *xanthus*. *Cell Motility*, *3*(3), 227–245. https://doi.org/10.1002/cm.970030304

408   Katz, Y., Tunstrom, K., Ioannou, C. C., Huepe, C., & Couzin, I. D. (2011). Inferring the structure
409   and dynamics of interactions in schooling fish. *Proceedings of the National Academy of*
410   *Sciences*, *108*(46), 18720–18725. https://doi.org/10.1073/pnas.1107583108

411   Keller, E. F., & Segel, L. a. (1970). Initiation of slime mold aggregation viewed as an instability.
412   *Journal of Theoretical Biology*, *26*(3), 399–415. https://doi.org/10.1016/0022-
413   5193(70)90092-5

414   Kessler, D. A., & Levine, H. (1993). Pattern formation in *Dictyostelium* via the dynamics of
415   cooperative biological entities. *Physical Review E*, *48*(6), 4801–4804.
416   https://doi.org/10.1103/PhysRevE.48.4801

417   Kolbinger, A., Gao, T., Brock, D., Ammann, R., Kisters, A., Kellermann, J., … Wetterauer, B.
418   (2005). A cysteine-rich extracellular protein containing a PA14 domain mediates quorum
419   sensing in *Dictyostelium discoideum*. *Eukaryotic Cell*, *4*(6), 991–998.
420   https://doi.org/10.1128/EC.4.6.991-998.2005

421   Kuzdzal-Fick, J. J., Fox, S. A., Strassmann, J. E., & Queller, D. C. (2011). High relatedness is
422   necessary and sufficient to maintain multicellularity in *Dictyostelium. Science*, *334*, 1548–
423   1551. https://doi.org/10.1126/science.1213272

424   Loomis, W. F. (2012). *The development of Dictyostelium discoideum*. Elsevier.

425   Loomis, W. F. (2014). Cell signaling during development of *Dictyostelium*. *Developmental*
426   *Biology*, *391*(1), 1–16. https://doi.org/10.1016/j.ydbio.2014.04.001

427   Martínez-García, R., & Tarnita, C. E. (2016). Lack of ecological and life history context can create
428   the illusion of social interactions in *Dictyostelium discoideum*. *PLoS Computational Biology*,
429   *12*(12), e1005246.

430   Martínez-García, R., & Tarnita, C. E. (2017). Seasonality can induce coexistence of multiple bet-
431   hedging strategies in *Dictyostelium discoideum* via storage effect. *Journal of Theoretical*
432   *Biology*, *426*, 104–116.

433   Palsson, E., & Othmer, H. (2000). A model for individual and collective cell movement in
434   *Dictyostelium discoideum*. *Proceedings of the National Academy of Sciences of the United*

435   *States of America*, *97*(19), 10448–10453.

436   Peleg, O., Peters, J. M., Salcedo, M. K., & Mahadevan, L. (2018). Collective mechanical
437   adaptation of honeybee swarms. *Nature Physics*, *14*(12), 1193–1198.
438   https://doi.org/10.1038/s41567-018-0262-1

439   Pluen, A., Netti, P. A., Jain, R. K., & Berk, D. A. (1999). Diffusion of macromolecules in agarose
440   gels: Comparison of linear and globular configurations. *Biophysical Journal*, *77*(1), 542–552.
441   https://doi.org/10.1016/S0006-3495(99)76911-0

442   Sawai, S., Thomason, P. A., & Cox, E. C. (2005). An autoregulatory circuit for long-range self-
443   organization in *Dictyostelium* cell populations. *Nature*, *433*(7023), 323–326.
444   https://doi.org/10.1038/nature03228

445   Simpson, S. J., McCaffery, A. R., & Hägele, B. F. (1999). A behavioural analysis of phase change
446   in the desert locust. *Biological Reviews*, *74*(4), 461–480. https://doi.org/10.1111/j.1469-
447   185X.1999.tb00038.x

448   Song, L., Nadkarni, S. M., Bödeker, H. U., Beta, C., Bae, A., Franck, C., … Bodenschatz, E.
449   (2006). Dictyostelium discoideum chemotaxis: threshold for directed motion. *European
450   Journal of Cell Biology*, *85*(9–10), 981–989. https://doi.org/10.1016/j.ejcb.2006.01.012

451   Stenhouse, F. O., & Williams, K. L. (1977). Patterning in *Dictyostelium discoideum*: The
452   proportions of the three differentiated cell types (spore, stalk, and basal disk) in the fruiting
453   body. *Developmental Biology*, *59*(2), 140–152. https://doi.org/10.1016/0012-
454   1606(77)90249-4

455   Strassmann, J. E., & Queller, D. C. (2011). Evolution of cooperation and control of cheating in a
456   social microbe. *Proceedings of the National Academy of Sciences*, *108*, 10855–10862.
457   https://doi.org/10.1073/pnas.1102451108

458   Strassmann, J. E., Zhu, Y., & Queller, D. C. (2000). Altruism and social cheating in the social
459   amoeba *Dictyostelium discoideum*. *Nature*, *408*(6815), 965–967.
460   https://doi.org/10.1038/35050087

461   Tarnita, C. E., Washburne, A., Martínez-García, R., Sgro, A. E., & Levin, S. A. (2015). Fitness
462   tradeoffs between spores and nonaggregating cells can explain the coexistence of diverse
463   genotypes in cellular slime molds. *Proceedings of the National Academy of Sciences*,
464   201424242.

465   Wolf, J. B. B., Howie, J. A. A., Parkinson, K., Gruenheit, N., Melo, D., Rozen, D., & Thompson,
466   C. R. L. (2015). Fitness trade-off result in the illusion of social success. *Current Biology*,
467   *25*(8), 1086–1090. https://doi.org/10.1016/j.cub.2015.02.061

468   Yuen, I. S., & Gomer, R. H. (1994). Cell density-sensing in *Dictyostelium* by means of the
469   accumulation rate, diffusion, coefficient and activity threshold of a protein secreted by starved
470   cells. *Journal of Theoretical Biology*, *167*, 273–282.

471

477   **Author contributions:** All authors contributed to the conception of the study. FWR, AES and TG
478   designed the experiments with input from RMG and CET. FWR performed the experiments with
479   initial guidance from AES. FWR analyzed the experiments. RMG developed the theoretical

480 models with input from FWR and CET. RMG performed and analyzed the simulations. RMG and
481 CET produced analytical calculations. CET drafted the paper, and all authors provided comments.
482
483 **Competing interests:** Authors declare no competing interests.
484
485 **Data and materials availability:** The data sets generated and analysed during the current study
486 are available in the Dryad repository at http://dx.doi.org/XXX. The computer code is available
487 from the corresponding authors upon request.

Materials and Methods

488

489 **Experiments.** *D. discoideum* **growth and plating**.
490   NC28.1, NC34.1, and NC85.2 —three clonal lineages of *D. discoideum* originally isolated from
491 Little Butt's Gap, North Carolina (Francis & Eisenberg, 1993) –were obtained from dictyBase
492 (Fey, Dodson, Basu, & Chisholm, 2013) and grown *on Klebsiella aerogenes* lawns prepared on
493 SM agar plates (Fey, Kowal, Gaudet, Pilcher, & Chisholm, 2007). After the *D. discoideum* cells
494 aggregated and formed fruiting bodies, spores were harvested and used to inoculate 3mL of a *K.*
495 *aerogenes* suspension in SorMC buffer (OD600 of 8). The suspension was kept in a shaker for 24
496 hours and then used to inoculate 12mL of the *K. aerogenes* suspension. During growth*, D.*
497 *discoideum* cell densities were kept below 3 x 10^6 cells/mL. After 24 more hours, in preparation
498 for the synchronous starvation of the cells, the suspension was cooled to 4°C for five minutes. The
499 suspension was then centrifuged at 700 g for three minutes at 4°C and the remaining pellet was
500 resuspended in 10mL of SorMC buffer. The spinning and resuspension cycles were repeated three
501 times to wash away any remaining *K. aerogenes* cells (Fey et al., 2013). For the final resuspension
502 the cell concentration was 10^7 cells/mL.
503 From each stock suspension, a dilution series in SorMC buffer (80%,70%,...,20%) was obtained.
504 In addition, a 5% dilution was prepared from each stock suspension. The 5% dilutions were below
505 the critical aggregation density, and they were used to estimate the total amount of cells in the
506 other samples coming from the same stock suspension. Cells were platen on non-nutrient agar gels
507 (2%, 3% and 4% concentrations) cast in 1.5mm acrylamide gel casts (Bio-Rad). Each of the diluted
508 and undiluted cell suspensions was applied to the agar substrates as a 10μL droplet.

509 The samples were then left to develop in a moist dark chamber at 21°C until the streaming phase
510 of aggregation was over and most of the aggregates were already at the slug stage (~14 hours).
511 Development was then halted by lowering the chamber temperature to 4°C. Even though the 5%
512 diluted suspension samples never aggregated, they were also left in the chamber for the full length
513 of the experiment. This circumvents the problem of residual divisions post resource removal. The
514 diluted and non-aggregated samples were then used to estimate the total number of cells in the
515 undiluted aggregated samples.

516 In order to check for the consistency of the dilution procedure, 5%, 10% and 15% dilutions of
517 NC34.1 strain stock solutions were also prepared and plated on 3% agar substrates. A linear
518 Gaussian model with intercept 0 was fit to the cell counts of different dilutions of the same
519 suspension. The standard deviation of this model was taken to be the error intrinsic to the dilution
520 process (Figure S2a).

521 For mixed strain experiments, strains NC28.1 and NC85.2 were used. They were grown, washed
522 and resuspended separately. Then, without diluting the suspensions, different mixes were made
523 (25%,50% and 75% of the initial strain NC28.1 suspension). A 5% dilution was made for each of

524 the two pure strain suspensions. Each of the mixes, pure strain suspensions, and dilutions were
525 plated as four replicates for each experiment. These 5% dilutions were used to estimate the
526 proportions of cells of each strain in each of the experiments. 3% agar substrates were used.

527 For the resource depletion experiments, cells of strains NC28.1 and NC85.2 were grown in
528 bacterial suspensions until they reached either a density of 1×10^6 cells per mL (conditions under
529 which bacteria were still plentiful), or for 10 hours longer than that (conditions under which
530 bacteria have just been depleted). In both treatments, cells were then washed from bacterial
531 leftovers and let aggregate on 3% agar gels

Imaging samples and counting cells.
533 An ultrasonic atomizer (from CVS) was used to uniformly apply a 0.5mm thick layer of warm
534 imaging solution (SorMC containing 0.3 mol/L of dextrose and 0.05% agar) to the samples. After
535 resting for 10 minutes at room temperature cells assume a spherical shape and detach from
536 neighboring cells. Samples were then photographed with a Canon t5i DSLR camera at a Nikon Ti-
537 Eclipse inverted microscope equipped with a 10X objective. The imaged area, a square of side
538 1.5cm, was large enough to encompass the initial cell plated area plus a buffer zone that ensures
539 that all cells were imaged. Custom software using the OpenCV package for Python was then used
540 to count the cells that did not join aggregation centers.

541 The error of automatic cell counts was estimated by taking samples of images of cells in various
542 densities, manually and automatically counting them and fitting a linear Gaussian model with slope
543 1 and intercept 0 (Figure S2b). The standard deviation of the fitted model was taken as the
544 automatic counting error.

545 Total plated cell counts in each sample were estimated by counting the non-aggregated 5% dilution
546 of the corresponding stock suspension and multiplying by the dilution factor of that particular
547 sample. We do not assess differential loner viability, which might effectively increase the
548 difference in loner allocation between strains.

Spatial pattern analysis.
550 For each cell in each experiment, the local cell density was calculated in a neighborhood with a
551 radius of 10% of the total experimental radius. Cells that weren't within the center of the
552 experimental area (defined by a radius of 60% of the total experimental radius) weren't included
553 in the analysis, to avoid border effects. For each strain and agar concentration, neighborhood
554 densities of cells of all experiments were pooled together in a probability distribution. The results
555 were qualitatively similar for other neighborhood radii, but because the imaging treatment might
556 shift a bit the position of the cells, we chose a radius that is considerably larger than this effect

Statistical analyses of mixed strain experiments. Given a constant initial cell density, we intend
558 to test if the loner-aggregator partitioning process of a strain is influenced by the genotypic identity
559 of its neighbors. We let P_i be the proportion of cells of strain i that stay as loners. We determined
560 that this depends on ρ_0, the initial density of the population, such that the density of loners in a
561 clonal population of strain i at density ρ_0 is $\rho_L^i = \rho_0 P_i(\rho_0)$. Here we investigate whether in mixes
562 P_i is also a function of the fraction $\Pi_j = 1 - \Pi_i$ of cells of co-occurring strain j (where Π_i is the
563 fraction of cells of strain i). The total loner density in the mix can be expressed as $\rho_L^{mix} =$
564 $\Pi_i \rho_0 P_i(\rho_0, \Pi_j) + \Pi_j \rho_0 P_j(\rho_0, \Pi_i)$, where ρ_0 is the initial total density of plated cells and Π_i is the
565 fraction of strain i in the initial mix.

13

Null hypothesis. If P_i is not a function of Π_j, then $\rho_L^{\mathrm{mix}} = \Pi_i \rho_L^i + \Pi_j \rho_L^j$, which is the linear combination of the expected loner counts for each of the strains composing the mix (null hypothesis).

Statistical test 1. Piecewise linear regression (Fig. 3). We measure departures from this linear expectation by fitting a piecewise linear regression to the data. The p-value shows how often data drawn from the global linear fit generates piecewise linear regressions with more extreme inclinations.

Statistical test 2. Maximum likelihood (Fig. S6a-c). We also use a maximum likelihood based model selection to test for non-linearity. We let $\rho_L^{\mathrm{mix}} = \rho_L^i + f(\Pi_j)(\rho_L^j - \rho_L^i) + \epsilon$ where f is the function of interest and ϵ is a normally distributed noise term. If $f(\Pi_j) = \Pi_j$ then we recover the null hypothesis. In addition, for f we explore three other functional forms: sigmoidal, convex and concave, which are given by a shape parameter a as follows:

$$f(\Pi_j) = \frac{a\Pi_j}{1+(a-1)\Pi_j} \quad - \quad \text{convex if } 0 < a < 1; \text{ concave if } a > 1$$

$$f(\Pi_j) = \frac{I_a(\Pi_j) - I_a(0)}{I_a(1) - I_a(0)} \quad \text{where} \quad I_a(x) = \frac{1}{1+e^{-a(x-0.5)}} \quad - \quad \text{sigmoidal}$$

We also considered three forms for the noise term: a homoscedastic structure, a constant coefficient of variation and a heteroscedastic structure, given respectively by

$$\epsilon \sim N(0, c)$$

$$\epsilon \sim N\left(0, \frac{c}{\rho_L^i + f(\Pi_j)(\rho_L^j - \rho_L^i)}\right)$$

$$\epsilon \sim N(0, c_i\Pi_i + c_j\Pi_j)$$

We computed the ΔAIC, the difference in AIC (Akaike Information Criterion) between a given model and the best model in the candidate set. Credible intervals were built for the shape parameter *a* using Log-likelihood ratios.

Statistical test 3. Bootstrapping analysis (Fig. S6d,e). For each of the five strain mix proportions, empirical distributions were bootstrapped and 50.000 data sets were constructed. For each resampled data set, a linear regression was performed using only the pure strain experiments and another linear regression was performed using only the mixed strain experiments. The difference between these inclinations is a measure of the non-linearity of the data set.

Theory. Population-partitioning model. We implement the spatially-explicit developmental model on a square system of lateral length $\ell = 0.2$cm that represents a single aggregation territory. Time is discretized in short intervals of length $dt = 0.01$h; our results are independent of the value of dt. Within each time step, the internal state and the position of every cell can be updated. Since reproduction and death are negligible over the temporal scales of aggregation, the total population size is conserved during each run of the model.

Consistent with the experimental setup, we initialize the simulations immediately after resource exhaustion with N_0 discrete and randomly distributed cells, assumed to be in a pre-aggregating state, P. Thus the initial density of cells is $\rho_0 = N_0/\ell^2$. P-cells do not move; they emit signal at a constant strain-specific rate γ and sense it with a strain-specific sensitivity threshold θ. The

14

608 assumption that *P*-cells do not move is consistent with experimental results showing a reduced
609 movement of vegetative cells at high density (D'Alessandro et al., 2018). Within each time step
610 *dt*, *P*-cells that sense a local signal density higher than the strain-specific sensitivity threshold *θ,*
611 may become aggregating *A*-cells with a strain-specific probability *λdt*. A detailed description of
612 how signal density is obtained at the position of each cell is below.

613 *A*-cells move in the direction of the aggregation center, which is exogenously imposed in the center
614 of the system, making a straight displacement of length *vdt* in every time step. This movement
615 pattern simplifies the complexities of *D. discoideum* motion during aggregation, such as the
616 tortuosity in single-cell trajectories caused by imperfect chemotaxis (Fisher, Merkl, & Gerisch,
617 1989). However, the net effect of these ingredients is to increase the time required to reach the
618 aggregation center, which can be incorporated in the model by changing the value of cell velocity.
619 *A*-cells stop sensing signal but they continue to emit it at the same strain-specific rate, *γ*. When *A*-
620 cells cross the location of the aggregation center (center of the system) in one of their
621 displacements, they adhere to the mound and become multicellular, *M*-cells. *M*-cells do not move
622 and they neither emit nor sense signal. Both the *A*-to-*P* and the *P*-to-*M* transition between cell
623 states are irreversible.
624 Simulations are allowed to run until the time between two consecutive cell arrivals to the mound
625 is larger than a fixed value $t_{arr} = 1$ hour. Alternatively, we explore the effect of a fixed aggregation
626 time by finalizing the simulations after an exogenously imposed time (results not shown). Neither
627 qualitative nor quantitative differences were observed between these two ending conditions,
628 provided that both of these times were sufficiently large. We compute the final density of loners
629 by counting the number of cells that do not belong to the mound at the end of each model
630 realization and dividing it by the area of the system, ℓ^2. Due to the low skewness of the distribution
631 of loner densities obtained from independent realizations, we use the mean loner density, which is
632 obtained by averaging over 100 realizations. A summary of the model parameterization is provided
633 in Table S1.

634 *Computation of signal density.* Signal is released by both *A*- and *P*-cells, but it is sensed only by
635 *P*-cells. The signal density, *σ*, at time *t* at the position *r* of a focal *P*-cell is

$$\sigma(\boldsymbol{r}, t) = \sum_{\boldsymbol{r}' \neq \boldsymbol{r}} \sigma_{\boldsymbol{r}'}(|\boldsymbol{r} - \boldsymbol{r}'(t)|) \tag{1}$$

636 where the index of the sum runs over the locations of all other *A*- and *P*-cells in the system,
637 $|\boldsymbol{r} - \boldsymbol{r}'(t)|$ is the distance between the focal cell and these other cells, and $\sigma_{\boldsymbol{r}'}$ gives the individual
638 contribution of a cell at location $\boldsymbol{r}'$ to the total signal density. Since *P*-cells do not move, $\boldsymbol{r}$ does
639 not depend on *t*; similarly, $\boldsymbol{r}'(t)$ is either constant (if it is the position of another *P*-cell) or not (if
640 it is the position of an *A*-cell). Our assumptions that signal is continuously released by each cell at
641 a strain-specific rate *γ,* diffuses in the system with diffusion constant *D* and spontaneously decays
642 at rate *η*, lead to a stationary profile in which signal density decreases with the distance from the
643 emitter (see SI Appendix for a detailed calculation of this profile

$$\sigma_{\boldsymbol{r}'}(|\boldsymbol{r} - \boldsymbol{r}'(t)|) = \frac{\gamma}{2\pi D} \mathrm{K}_0\left(\sqrt{\frac{\eta}{D}}|\boldsymbol{r} - \boldsymbol{r}'(t)|\right). \tag{2}$$

644 *K_0* is the zero-order modified Bessel function of the second kind. Since in the experiments
645 aggregation occurs simultaneously on several adjacent aggregation territories, signals may diffuse

15

646 from one territory to another. To allow for this possibility in the model, the distances between the
647 sensing focal P-cell and each of the emitters are measured using periodic boundary conditions.

Competition model.

649 This model consists of a sequence of growth-starvation periods with the population partitioning
650 between loners and aggregators occurring at the onset of starvation. The expected length of the
651 starvation periods (i.e., mean starvation time) defines the environmental conditions. We discretize
652 each environment into $\# = 10^4$ isolated patches (no cell dispersal between them) of area 1 and
653 identical environmental conditions. The model architecture broadly follows (Martínez-García &
654 Tarnita, 2016) but the population partitioning between loners and aggregators is modified to
655 incorporate the behavior produced by the developmental model described above. We assume that
656 the loner-aggregator partitioning curve is constant for all starvation events. Therefore, we do not
657 consider mutation or horizontal gene transfer, which could alter strains' aggregation behavior.

658 *Growth.* During growth, free-living amoebae of two different strains compete for a shared resource
659 within each patch. The initial frequency of each strain in the mix is drawn from a standard log-
660 normal distribution, and the total initial population size X_0 is normalized to the size of the resource
661 pulse, R_0. The size of the resource pulse is fixed and large to guarantee that the population of cells
662 in the patch is also large and that its fluctuations do not affect the aggregator-loner partitioning
663 (i.e., aggregation occurs for population sizes that lie in the region in which loner density plateaus
664 in Fig. S4). Mathematically, the growth dynamics is given by a Monod-like equation:

$$\dot{X}_i = \frac{cR}{R + R_{1/2}} X_i \quad (i = 1,2) \qquad (3a) \qquad \dot{R} = \frac{-cR}{R + R_{1/2}} \sum_{i=1}^{2} X_i, \qquad (3b)$$

665 where the dot indicates the time derivative, X_i is the population size for strain i, R is the amount of
666 resources, and $R_{1/2}$ is the abundance of resources at which the growth rate is half of its maximum
667 c. Here, for simplicity, we assumed that both strains have the same maximum growth rate, although
668 relaxing this assumption constitutes an important expansion towards a more complete
669 understanding of life history traits and tradeoffs in slime molds (Martínez-García & Tarnita, 2016,
670 2017; J.B.B. Wolf et al., 2015). The growth phase finishes when resources are below a starvation
671 threshold ($R^* = 1$) that is exogenously imposed, since R only tends to zero asymptotically in Eq.
672 (3b).

673 *Population partitioning.* Since cell death is negligible over the temporal scales of aggregation, we
674 assumed that the aggregator-loner partitioning occurs instantaneously upon resource exhaustion.
675 We explored two different scenarios:

676 (a) Well-mixed development. Each patch is occupied by a homogenous mix of the two strains
677 (Figure S8). Upon resource exhaustion, the density of loners left behind by each of the two
678 strains is determined from the pair-specific co-developmental curve obtained via simulations
679 of co-development using the spatially-explicit developmental model above (Fig. S7a,c).
680 Whenever the composition of the mix at the end of a growth period does not coincide with
681 any of the proportions sampled with co-developmental simulations, we estimate the density
682 of loners of each strain with a linear interpolation between the two closest points to the
683 desired proportion. Finally, since both strains are homogeneously distributed across the
684 whole patch of area 1, the number of loners of each strain i, X_i^L (which is the variable of
685 interest for our model), is identical to loner density. We obtain the number of aggregated

16

686   cells of each strain as the difference between that strain's population size upon resource
687   exhaustion (immediately before the population partitioning) and its number of loners.

688   (b) Segregated development. Each patch is occupied by the two strains but they do not mix; we
689   therefore assume that they occupy a fraction of the patch area equal to that strain's proportion
690   (Fig. S8). Upon resource exhaustion, the density of loners left behind by each of the two
691   strains is determined from simulations of the developmental model above under clonal
692   conditions. To obtain the number of loners, we multiply the density by the fraction of the
693   patch (of area 1) occupied by that strain. We then obtain the number of aggregated cells as
694   in the well-mixed scenario.

695   After the population partitioning occurs, based on experimental measures that consistently find an
696   80:20 spore:stalk ratio within *D. discoideum* fruiting bodies formed under identical conditions
697   (Stenhouse & Williams, 1977), we multiply the number of aggregated cells of each strain i by the
698   same constant factor $s = 0.8$ that reflects the effect of spore-stalk cell differentiation. This operation
699   yields the number of reproductive spores, X_i^{SP}.

700   *Starvation.* The population partitioning is followed by a starvation period of length T_{st}, in which
701   both aggregated and non-aggregated cells die, but at different rates. Spores die at a constant and
702   low rate δ, whereas loners have a survival probability, S, that decays with time and reaches zero at
703   a maximum survival time T_{sur}. Analogous with (Martínez-García & Tarnita, 2017), we fit this
704   maximum survival time as well as the functional shape of the survivorship curve using
705   experimental data (Dubravcic, 2013) to obtain
706

$$S(t) = \frac{e^{-(\mu t)^\varsigma} - e^{-(\mu T_{sur})^\varsigma}}{1 - e^{-(\mu T_{sur})^\varsigma}}, \tag{4}$$

707

708   where μ is the rate of decrease of the survival probability and ς is a parameter that modulates the
709   decay of S with time. At the end of the starvation phase, we obtain the populations of surviving
710   loners and spores of each strain i as
711

$$X_i^L(t + T_{st}) = X_i^L(t)S(T_{st}) \qquad (5a) \qquad X_i^{SP}(t + T_{st}) = X_i^{SP}(t)e^{-\delta T_{st}}. \tag{5b}$$

712

713   The lengths of the starvation periods T_{st} are either constant (deterministic environments, in which
714   the length of each starvation period coincides with its mean value) or drawn from an exponential
715   distribution with a mean $\bar{T}_{st}$ that gives the expected length of the starvation periods. We label
716   deterministic environments using the length of their starvation periods T_{st} and stochastic
717   environments using their expected value $\bar{T}_{st}$. $\bar{T}_{st}$ (or T_{st} in deterministic environments) is a
718   measure for the environmental quality. Lower values of $\bar{T}_{st}$ represent better environments in which
719   pulses of resources arrive more frequently on average; larger values of $\bar{T}_{st}$ represent worse
720   environments in which resources recover less frequently. Each starvation phase ends with the
721   arrival of the next resource pulse of size R_0. We assume that all loners have the same viability
722   regardless of strain (i.e. that different strains do not have differential loner mortality); therefore,
723   upon resource replenishment, all surviving loner cells start reproducing immediately, following
724   Eqs. (3). Spores take an additional time T_{ger} to germinate (Cotter & Raper, 1968), during which
725   they continue to die at rate δ. At the end of the germination time, not all spores become reproducing
726   cells; spores have a probability ω of germinating successfully (Dubravcic et al., 2014). Therefore,

727   we multiply the total number of spores by a constant factor ω to obtain the fraction of the
728   population of spores that become viable cells and start reproducing according to Eqs. (3).

729   We repeat this sequence of growth-starvation cycles until one of the strains becomes extinct. We
730   then record the winning strain for each patch and the time-to-extinction for the loser (proxy for
731   transient alpha-diversity). Once we have obtained the winner in each patch, we calculate the
732   variability in the winner across different patches, Φ (proxy for stationary beta-diversity), as

$$\Phi = \frac{\# - |\#_w - \#_b|}{\#}, \tag{6}$$

733   where $\# = 10^4$ is the total number of patches, and $\#_w$ and $\#_b$ are the number of patches dominated
734   by the worse, respectively the better aggregator in the stationary state. From Eq. (6), it follows that
735   Φ varies between 0 and 1 ($\Phi = 1$ when $\#_w = \#_b$ and $\Phi = 0$ when $\#_w = \#$ or $\#_b = \#$). Since the
736   extinction times and the noise in the extinction times and Φ vary depending on the pair of strains
737   and the environmental conditions, mean values are taken over a varying number of independent
738   realizations of the model to optimize computational efficiency. A summary of the model
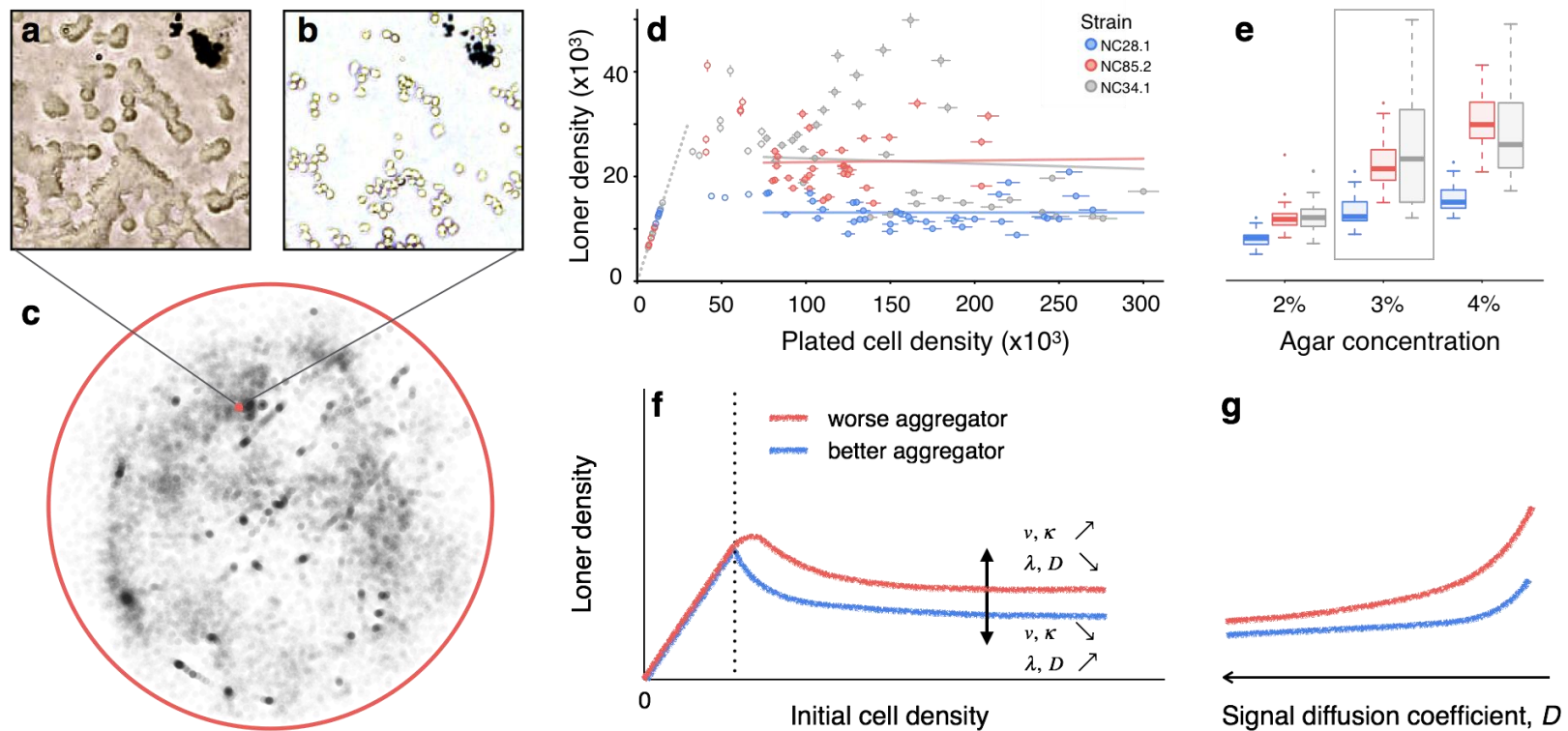739   parameterization is provided in Table S1.
740

Figure 1. Loners are a heritable component of *D. discoideum* fitness. a, b, After aggregation, loner cells are hard to individualize (**a**), but become clearly distinguishable after processing (**b**). **c,** Map of the position of each loner cell in an experiment (NC85.2 developing in 3% agar). Red square marks region shown in (**a,b**). **d,** Loner densities of three strains as a function of initial plated density in 3% agar. Error bars, independent estimates of counting error (see Methods). Lines correspond to linear regressions using only high-initial-density data points (filled circles, >75.000 cells/cm^2). **e,** Loner densities from experiments with high initial cell density as a function of substrate agar concentration (y-axis same as in **d**). Boxes, inter-quartile ranges; horizontal lines, medians; whiskers, 1.5× inter-quartile range from the median; points, outliers. Strain NC28.1 always left fewer loners (*t*-test, p<0.001). Values inside frame correspond to data used in (**d**). **f, g** Schematic of model results showing loner densities as a function of initial cell density (**f**) and signal diffusion coefficient (**g**). The y-axis in (**g**) is the same as in (**f**).
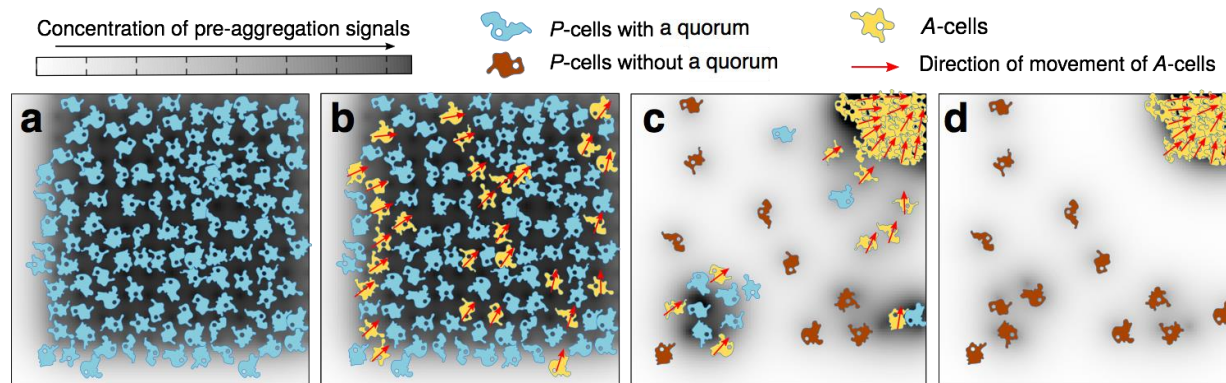
Figure 2. Developmental model schematic. a, At high initial densities, all *P*-cells have a quorum to initiate aggregation. **b,** With a strain-specific probability, some *P*-cells transition into *A*-cells. **c,** As *A*-cells aggregate, some of the *P*-cells that did not transition into *A*-cells are left without a quorum. These are the loners. **d,** At the end of development, *P*-cells far from the aggregate location are more likely to have been left without a quorum and to stay as loners.
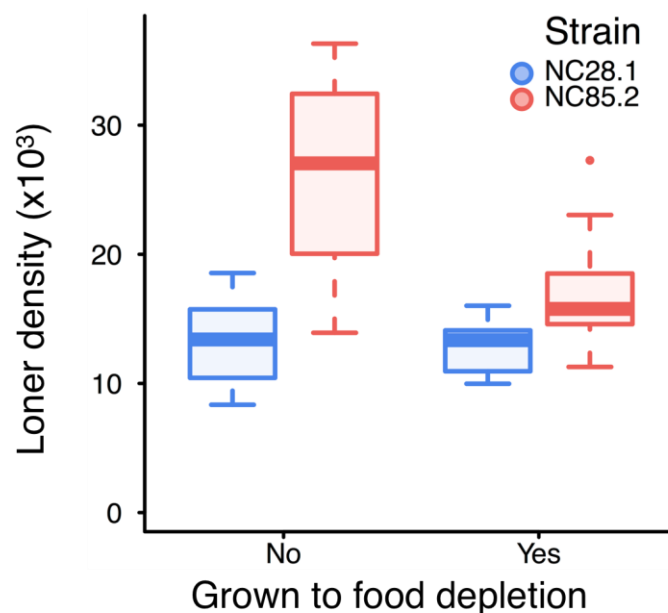

Figure 3. Well-mixed signaling changes loner behavior. Allowing cells to exhaust their resources in suspension does not significantly change the behavior of the better aggregator (strain NC28.1) (p = 0.7), but it reduces the mean and variance of the number of loners of the worse aggregator (strain NC85.2) (p = 0.0006). Boxes, inter-quartile ranges; horizontal lines, medians; whiskers, 1.5× inter-quartile range from the median; points, outliers.
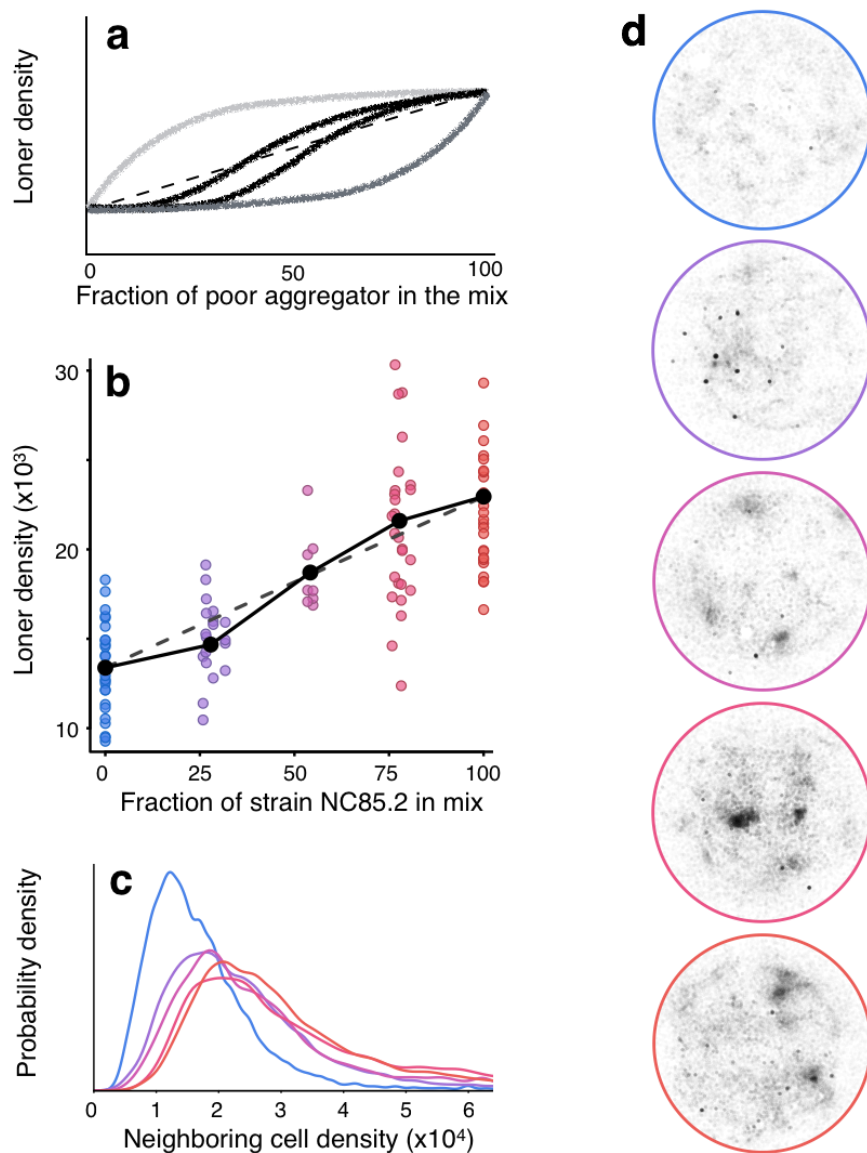
Figure 4. Co-occurring strains interact during development. a, Schematic of the range of theoretically predicted loner densities at different mix proportions of two co-occurring strains (thick curves). Dashed line, expected loner densities if cells commit to aggregation independent of the identity of their neighbors. **b,** Experimentally observed loner densities for different mix proportions of a better (NC28.1, blue) and a worse (NC85.2, red) aggregating strain in 3% agar. Black points, mean loner densities for each of the five proportions. Dashed line, same as in (**a**). Solid lines, piecewise linear regressions, which deviate significantly from the linear fit (p=0.019; see Methods). **c,** Experimentally observed spatial patterns of each mix proportion are characterized by the local cell density around each cell (see Methods). Narrower distributions (NC28.1, blue curve) correspond to more homogeneously distributed loners. Broader distributions (NC85.2, red curve) correspond to more clumped loners. **d**, Experimentally obtained loner position maps are shown for each of the mixed proportions. Colors in (**c,d**) correspond to colors in (**b**).
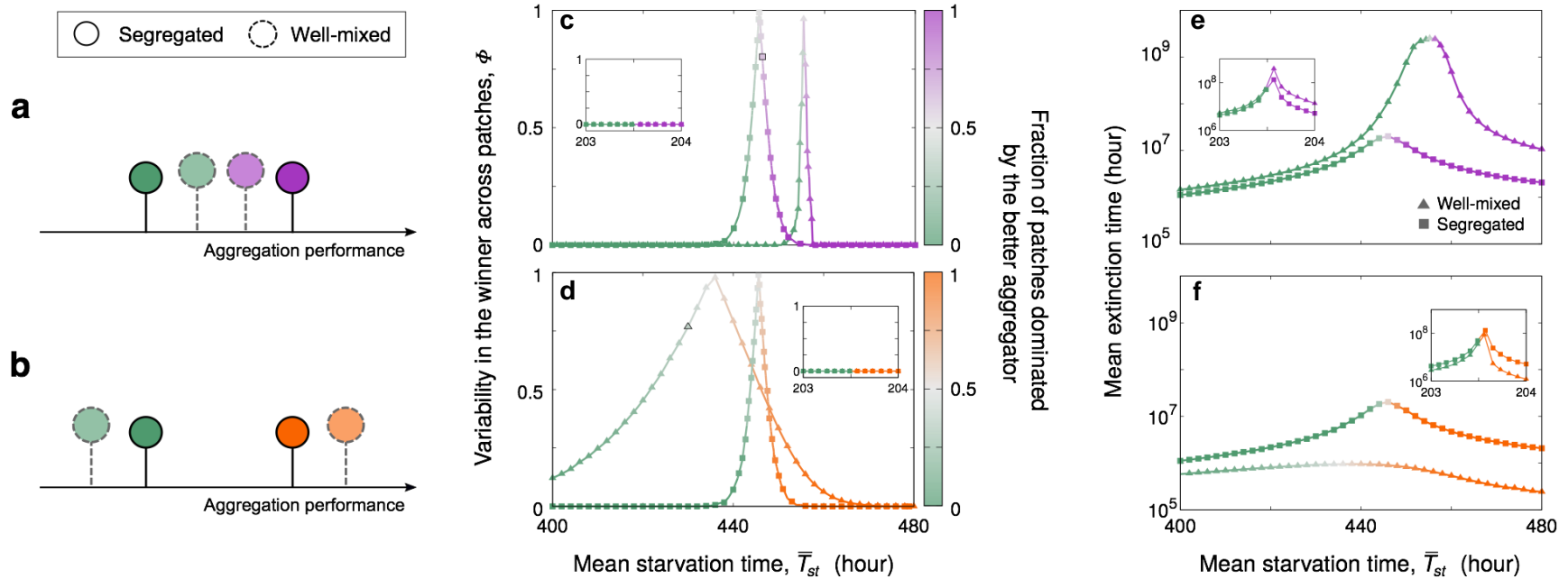
Figure 5. Ecological implications of developmental interactions. a, b, Co-development makes strains (different colors) more similar (**a**, case i) or more different (**b**, case ii) in their partitioning behavior. **c-f,** Effect of well-mixed versus segregated development on (**c, d**) the identity of the winner and (**e, f**) extinction times. Theoretical dynamics in the two environments whose symbols have a black boundary are shown in Fig. 6. Panels **c, e** and **d, f** are predictions for the pairs of strains in Figures S7a and S7c, respectively. Green strain is the same across all panels. Main panels, stochastic environments; insets, deterministic environments (see Methods). Color gradients indicate the change in the fraction of patches dominated by each of the mixed strains. Parameterization as in Fig. S7a,c

a Strains converge in their partitioning behavior (case i).
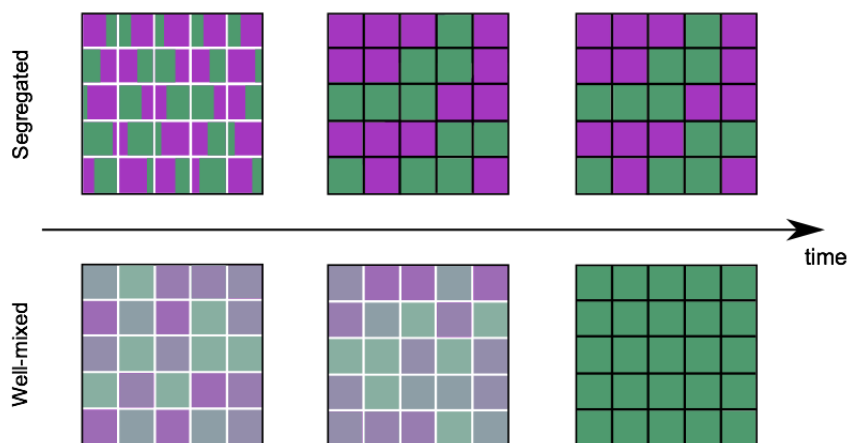
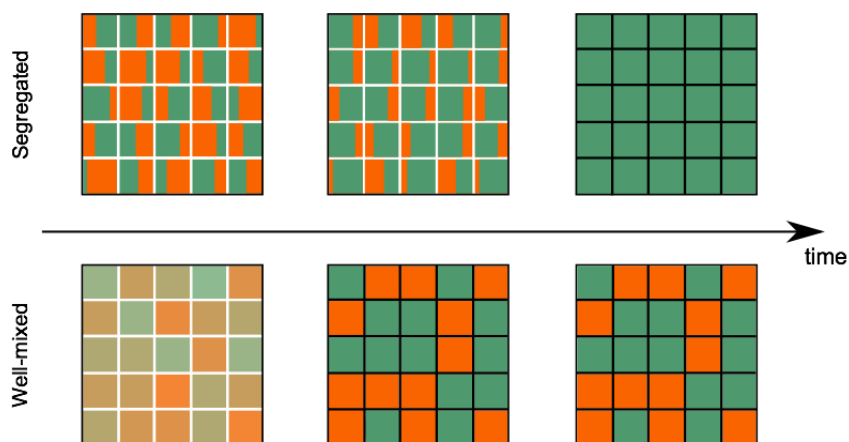**b** Strains diverge in their partitioning behavior (case ii).

Figure 6. Model results of the effects of developmental interactions on transient alpha-diversity and stationary beta-diversity. a,b, White interior boundaries symbolize a transient patch-level dynamic; black interior boundaries symbolize a stationary patch-level dynamic. a, Strains converge in their partitioning behavior due to developmental interactions (case i). In a stochastic environment with mean starvation time $\overline{T}_{st} = 448$ hour (symbol with black boundary in Fig. 4e), co-development induced quasi-neutrality increases transient coexistence (and transient alpha-diversity). However, it also eliminates the variability in the winner and thus co-development induced quasi-neutrality eliminates stationary beta-diversity. b, Strains diverge in their partitioning behavior due to developmental interactions (case ii). In a stochastic environment with mean starvation time $\overline{T}_{st} = 430$ hour (symbol with black boundary in Fig. 4e), co-development induced character displacement has the opposite effect from (a): the mean extinction time decreases (decreased transient alpha-diversity) but the variability in the winner across patches increases compared to segregated development (increased stationary beta-diversity).

23
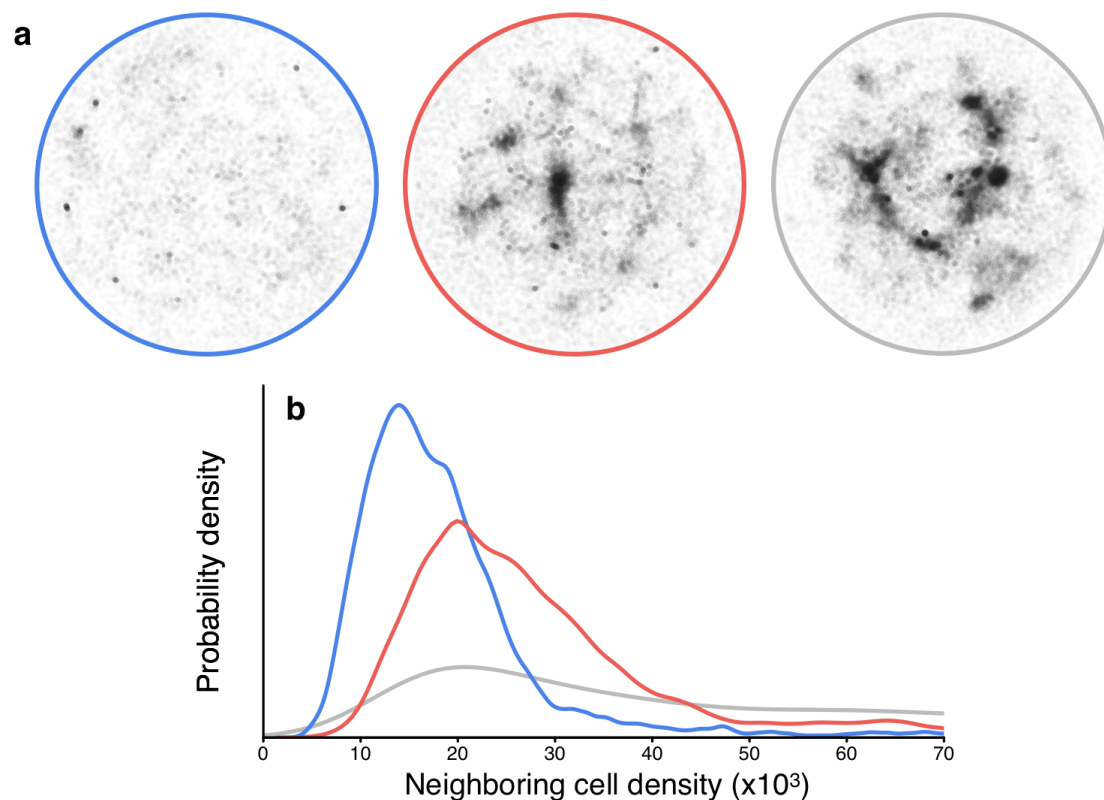
Figure S1. Experimental loner spatial distributions. a, Representative loner position maps are shown for each of the three strains (NC28.1 in blue, NC85.2 in red and NC34.1 in grey) plated on 3% agar. The position of each cell is plotted such that darker regions represent regions densely packed with loners. **b,** Characteristic loner spatial patterns for each strain are expressed as the probability distribution of local cell densities (see Methods). Broader peaks and fatter distribution tails (such as for NC34.1) correspond to more heterogeneously distributed loner cells.

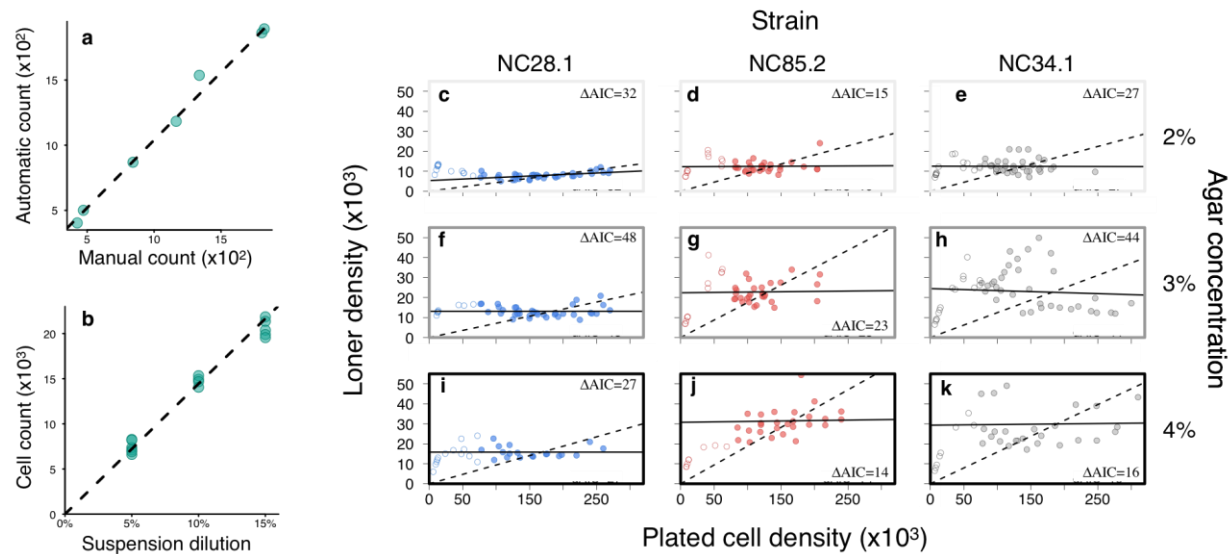**Figure S2. Experimental loner counts. a,** Loners in regions with varying loner densities were algorithmically counted and plotted against manual (by eye) counts for those same regions. Dashed line = automatic and manual counts coincide. The dispersion around the line is a measure of the counting error. **b,** Cell counts in experiments realized with dilutions from a same cell suspension. Cell densities were below the aggregation threshold. Dashed line = linear regression with intercept anchored at zero. The inclination is a measure of the cell density of the initial suspension, and the dispersion around the regression line is a measure of the error introduced whenever a dilution is made. **c-k,** Loner counts are shown as a function of initial cell plating densities for each of the three strains and each of the three substrate agar concentrations. For initial plating densities above 7.5×10^4 cells/cm2, aggregation occurs for all strains and substrates. To test if above this critical cell density the decision to aggregate is context-independent, those samples with high initial plating densities (filled circles) were used to fit linear Gaussian models with 0 intercept (dashed lines). These zero-intercept models were contrasted to linear Gaussian models with a free intercept parameter (solid lines). ΔAIC, the difference in AIC (Akaike Information Criterion) between the 0-intercept and free-intercept models, shows that the latter outperformed the former for all substrates and strains, indicating that the decision to aggregate is context-dependent. Moreover, the inclines of the best fitting linear models are not significantly different from zero for all but the best aggregating conditions (strain NC28.1 on 2% agar substrates), and even then only weakly positive. This indicates that loner densities plateau at high initial plating densities.
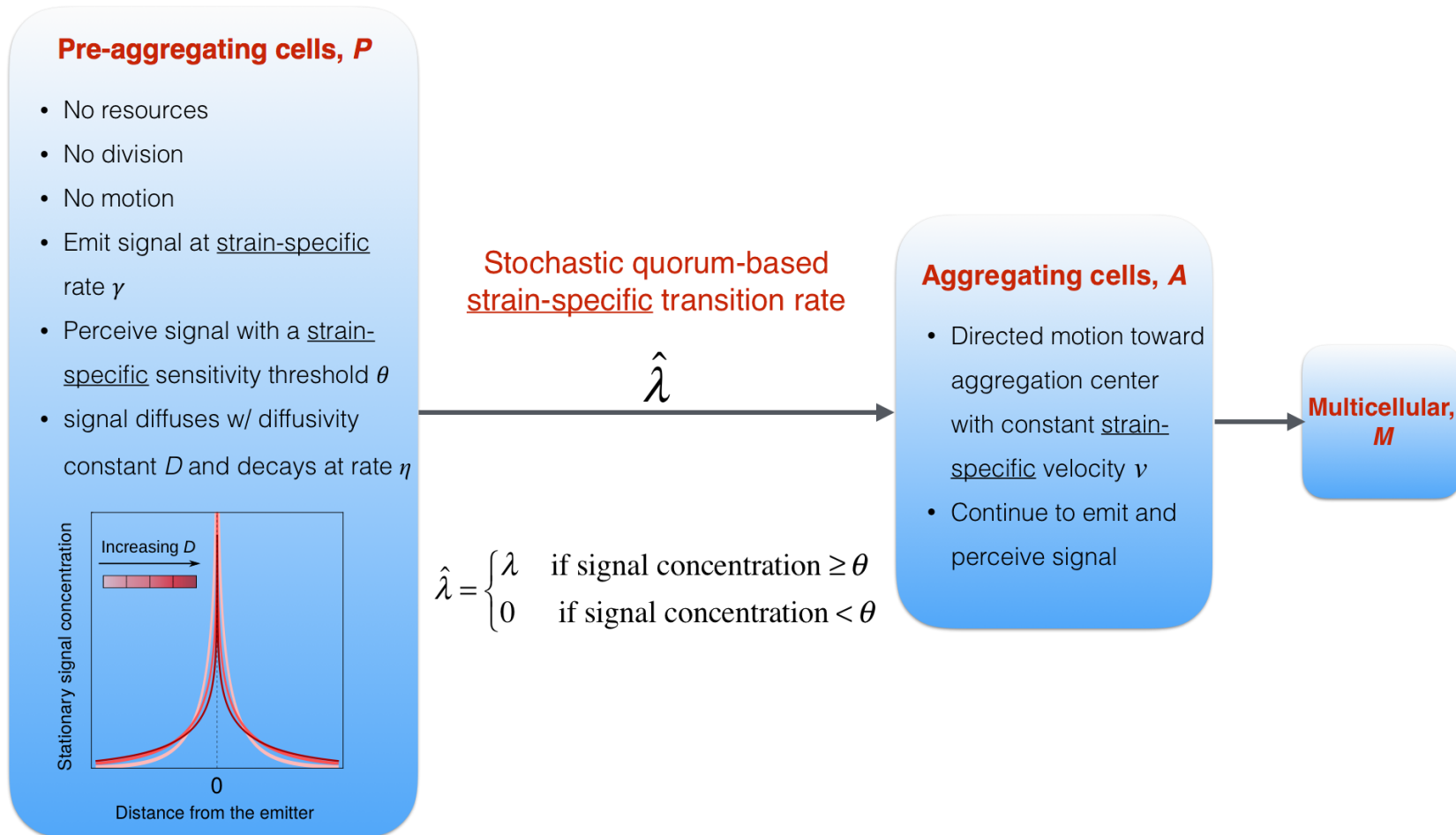
Pre-aggregating cells, *P*

- No resources
- No division
- No motion
- Emit signal at <u>strain-specific</u> rate γ
- Perceive signal with a <u>strain-specific</u> sensitivity threshold θ
- signal diffuses w/ diffusivity constant D and decays at rate η

Increasing *D*

Stationary signal concentration

0

Distance from the emitter

Stochastic quorum-based <u>strain-specific</u> transition rate

$\hat{\lambda}$

$$\hat{\lambda} = \begin{cases} \lambda & \text{if signal concentration} \geq \theta \\ 0 & \text{if signal concentration} < \theta \end{cases}$$

Aggregating cells, *A*

- Directed motion toward aggregation center with constant <u>strain-specific</u> velocity v
- Continue to emit and perceive signal

Multicellular, *M*

Figure S3. Schematic of the developmental model. We formulated an individual based model approach in which cells can be in three possible internal states: pre-aggregating, *P*; aggregating, *A*; and multicellular, *M*. Each state has different properties, listed in the blue boxes. The transitions between states occur only in one direction, as indicated by the grey arrows. The *P*-to-*A* transition is based on quorum sensing and it occurs at a strain-specific rate, λ; for each time step *dt*, if the density of signals is above the strain-specific sensitivity threshold, *P*-cells have a probability λdt of becoming *A*-cells. The transition from aggregation to multicellularity is entirely based on movement, and it occurs when cells arrive at the aggregation center.
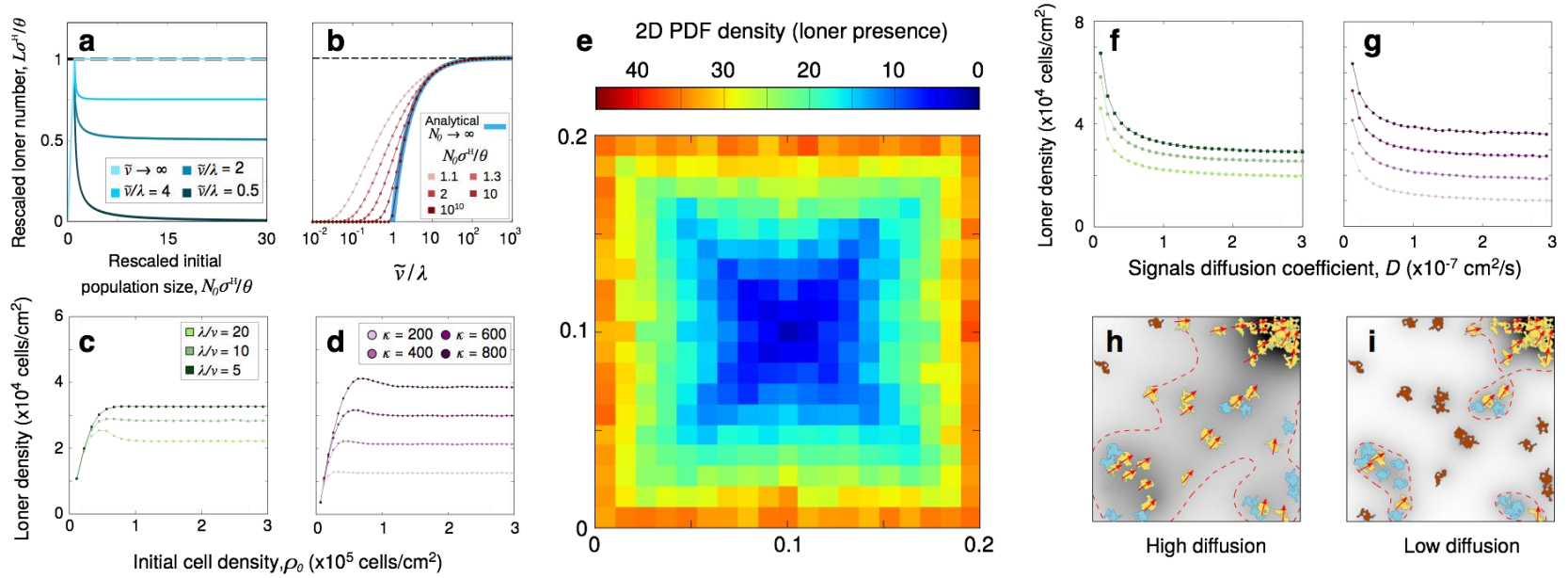
Figure S4. Model results for clonal development. a, Analytical solutions in the limit $D \to \infty$ for the rescaled number of loners versus the rescaled initial population size (Eqs. (2.13), (2.15), and (2.16) in the SI). **b**, Phase separation between perfectly synchronized (no loners) and asynchronized (loners) development in the limit $D \to \infty$. Red curves are obtained *via* numerical integration of Eqs. (2.11) and (2.12) in the SI for different initial population sizes; the blue-thick curve corresponds to the analytical result in the limit $N_0 \to \infty$ (Eq. (2.22) in the SI and Box 1 in the main text). **c, d**, Loner density versus initial cell density when (**c**) strains differ in λ/v with fixed $\kappa=500$ or (**d**) strains differ in κ with fixed $\lambda=1$ and $v=12\mu m/min$. $D=10^{-7}$. **e**, Probability density function for the presence of loners; the aggregation center is at the center of the system. The histogram is computed using the spatial positions of loners from 100 independent realizations of the model with $D=3\times10^{-8}$, $\rho_0=3\times10^5$, $\lambda=1$, $\kappa=400$. **f, g**, Loner density versus diffusion coefficient when: **f**, strains differ in λ/v with fixed $\kappa=500$; **g**, strains differ in κ with fixed $\lambda=1$ and $v=12\mu m/min$. **h, i**, Schematic representation of the reduction in the regions in which signal density is above the strain-specific sensitivity threshold as a result of reducing the diffusion coefficient. Dashed-red lines delineate the regions in which signal density is above a strain-specific sensitivity threshold. Color code for the cells and the concentration of signals as in Figure 2 (a-d). In (**a-g**), non-specified parameters and units are as in Table S1.
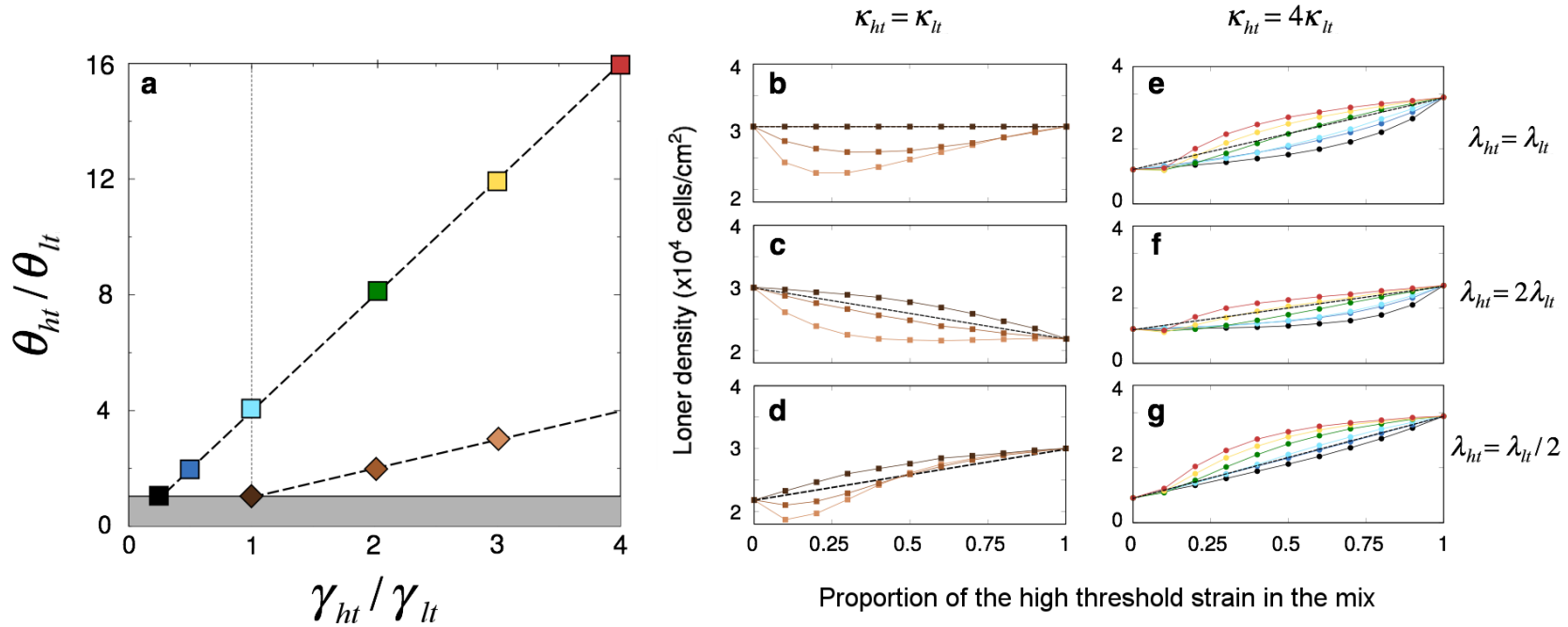
27

Figure S5. Model results for co-development. For a systematic exploration of the outcome of pairwise developmental interactions within the three-dimensional strain-specific parameter space (γ, θ, λ), strains in each mix are labeled according to their relative value of the sensitivity threshold, θ. We use the subindex lt, standing for 'low threshold', to label strain-specific parameter values of the strain with the lowest θ, and the subindex ht, standing for less sensitive, to label strain-specific parameter values of the strain with the highest θ. **a,** γ_{ht}/γ_{lt} — θ_{ht}/θ_{lt} parameter space ($\theta_{ht}/\theta_{lt} > 1$ by definition). The thick-dashed lines trace two transects of the parameter space in which $\kappa_{ht} = \kappa_{lt}$ (lower line) and $\kappa_{ht} = 4\kappa_{lt}$ (upper line). Densities of mixed loners are shown in (**b-d**) for the parameter values along the lower line and in (**e-g**) for parameter values along the upper line. Specific parameter relationships are indicated by the positions of the squares, whose color is maintained in the mixed-loner curves (**b-g**). **b-d,** $\kappa_{ht} = \kappa_{lt} = 600$, with $\theta_{ht} = 300$; and $\theta_{lt} = 300$ (darker brown), $\theta_{lt} = 150$ (brown), $\theta_{lt} = 100$ (lighter brown); **b,** $\lambda_{ht} = \lambda_{lt} = 1$; **c,** $\lambda_{ht} = 2$, $\lambda_{lt} = 1$; **d,** $\lambda_{ht} = 1$, $\lambda_{lt} = 2$. **e-g,** $\kappa_{ht} = 800$, with $\theta_{ht} = 400$ and $\kappa_{lt} = 200$ with $\theta_{lt} = 25, 33, 50, 100, 200, 400$ from top to bottom curve (red to black); **e,** $\lambda_{ht} = \lambda_{lt} = 1$; **f,** $\lambda_{ht} = 2$, $\lambda_{lt} = 1$; **g,** $\lambda_{ht} = 1$, $\lambda_{lt} = 2$. Dashed lines in (**b-g**) indicate the null hypothesis. Model parameterization shown in Table S1 with $D = 10^{-7}$ and $\rho_0 = 3 \times 10^5$. Averages taken over 100 independent model realizations.
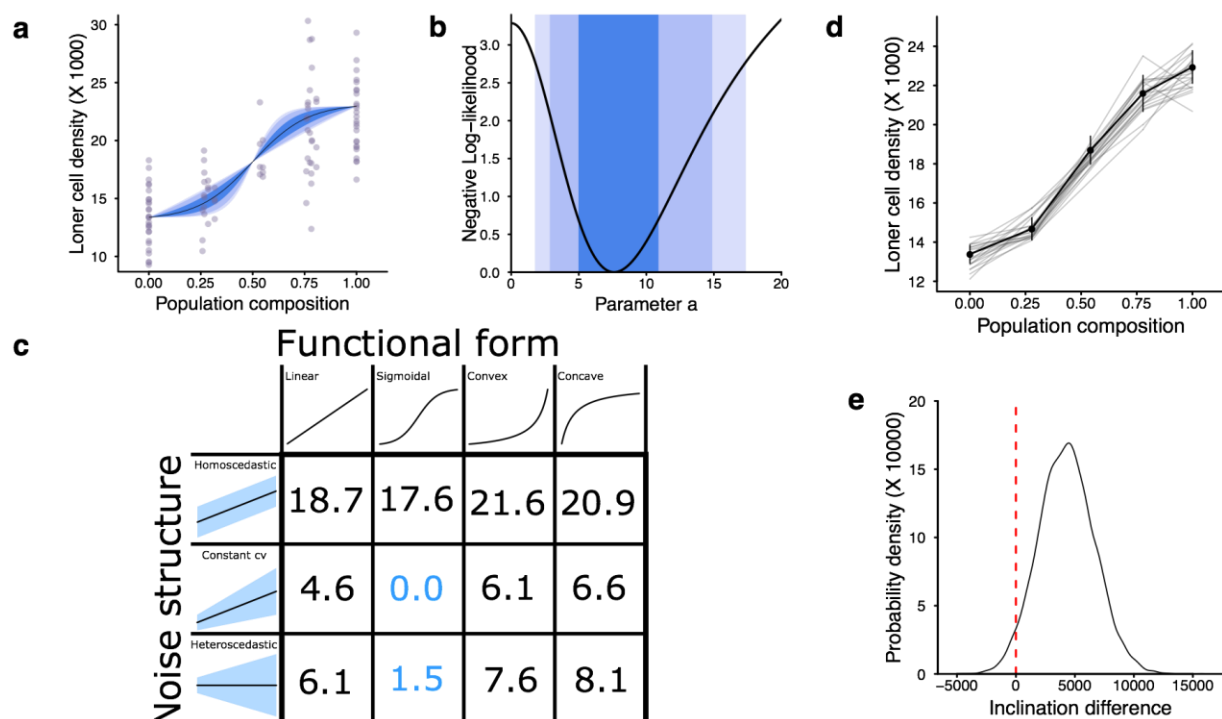
Figure S6. Statistical analysis of non-linearity in mixed strain experiments. a-c, Maximum likelihood analysis. a, Grey points = experimental mixed loner densities (see Fig. 3b). Black curve = expected loner densities for the maximum likelihood estimate of shape parameter a (see Methods). Blue areas = envelopes for the loner density curves for the confidence intervals defined by likelihood ratios of 2, 8 and 16, from darker to lighter. **b,** Negative Log-likelihood profile for the shape parameter a of the model with the best Akaike Information Criterion (AIC). Blue areas = confidence intervals defined as in (**a**). **c,** ΔAIC, the difference in AIC between a given model and the best model in the candidate set. Blue values = the two best-fitting models. **d,e, Bootstrapping analysis.** For each of the five strain mix proportions, empirical distributions were bootstrapped and 50.000 data sets were constructed. **d,** Grey lines = piecewise linear regressions of 20 of these resampled data sets. Black line = the mean of all resampled data sets. Error bars = standard errors. **e,** For each resampled data set, a linear regression was performed using only the pure strain experiments and another linear regression was performed using only the mixed strain experiments. The difference between these inclinations is a measure of the non-linearity of the data set. Black line shows the probability density function of these inclination differences. Red line at zero marks linearity (p=0.033).
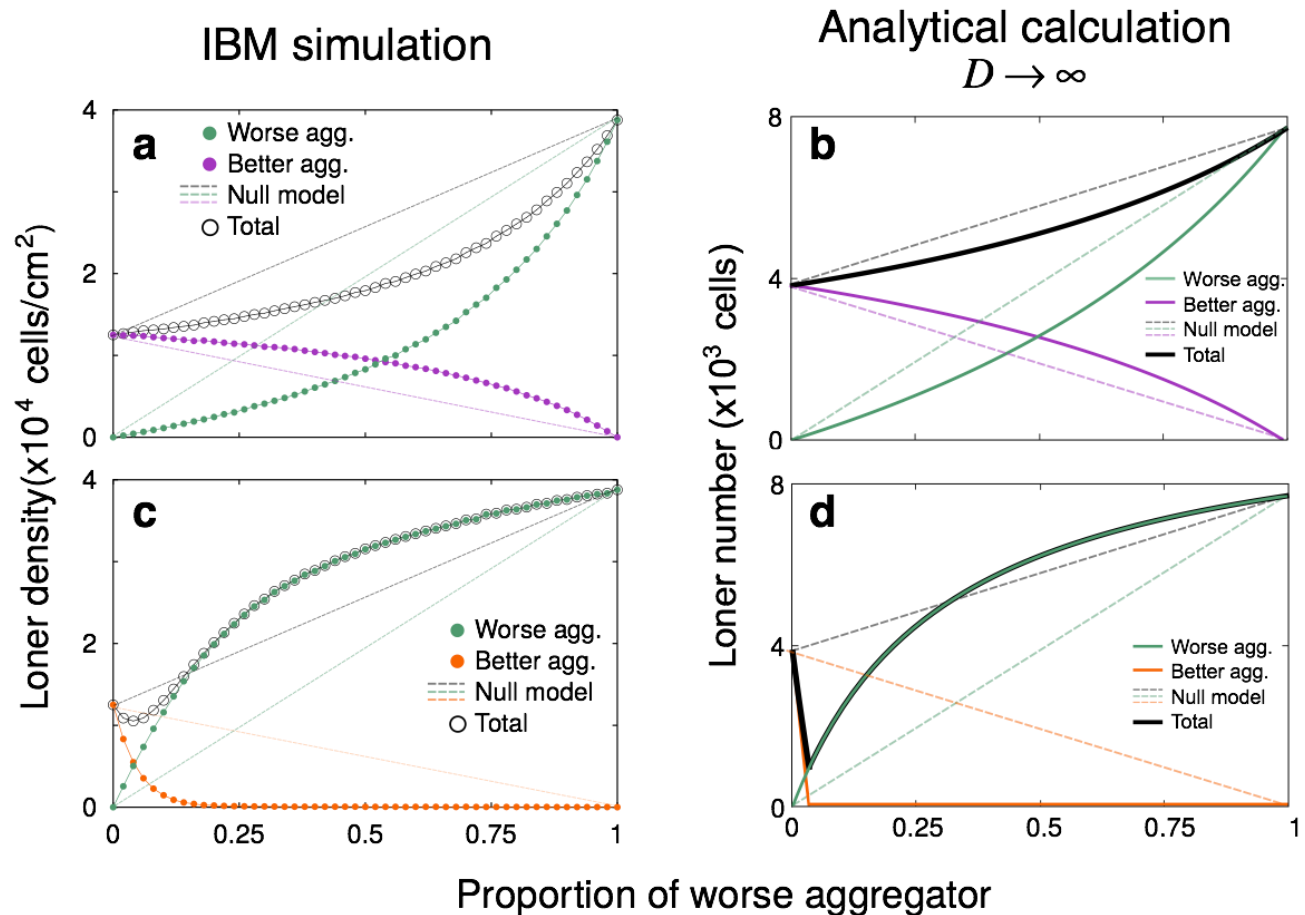
Figure S7. Model results for the effects of co-development on individual strains. Developmental interactions lead strains to become more similar (**a, b**) or more different (**c, d**). (**a, c**) Simulations of the individual based model, $D = 10^{-7}$. (**b, d**) The analytical approximations to (**a, c**) obtained in the limit $D \to \infty$ (Eqs. (2.31) and (2.33) in the Supplementary Information), qualitatively recapitulate the behavior of mixed-loners and of the loners of each strain. Parameterization: $\gamma_w = 0.5$, $\theta_w = 400$ ($\kappa_w = 800$), $\lambda_w = \lambda_b = 1$, $\kappa_b = 200$ with (**a**) $\gamma_b = 1$ and (**b**) $\gamma_b = 0.25$. w = worse aggregator; b = better aggregator. Remaining parameters are as in Table S1. The color code for each strain corresponds to Fig. 4.
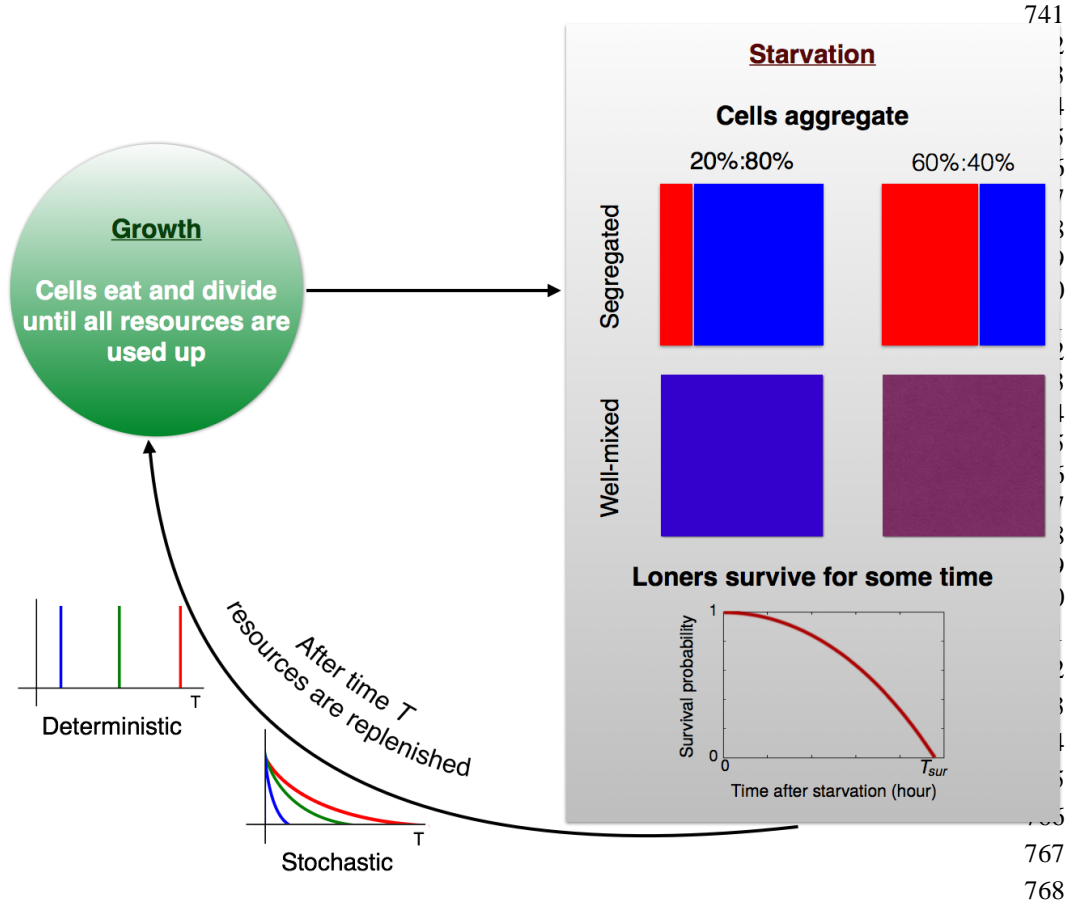
Figure S8. Schematic of the competition model. The model consists of a sequence of growth-starvation cycles. During growth, cells consume a shared pulse of resources and divide; during starvation, loners and aggregated cells die at different rates. The length of the starvation periods T_{st} can be either fixed (deterministic environments, defined by T_{st}) or drawn from an exponential distribution (stochastic environments, defined by the mean starvation time $\bar{T}_{st}$). Upon resource exhaustion (at the end of the growth period), the population partitions into aggregators and loners according to our population partitioning model. We compare two scenarios: *well-mixed*, where co-occurring strains co-develop and loner densities are obtained from co-development curves (e.g., as in Figure S7), or *segregated*, where strains are assumed to not mix and loners are derived from each strain's clonal development partitioning.

	Symbol	Definition	Units	Model value	Experimental observable	Exp. value	Ref.
	Theory				**Experiment**		
Population partitioning model	λ	Strain specific P-to-A transition rate	hour^{-1}	Varied	--		
	θ	Strain-specific sensitivity threshold	Kg/cm^2	Varied	--		
	γ	Strain-specific signaling rate	Kg/hour	Varied	--		
	v	Strain-specific A-cells velocity	μm/min	Varied around 12	Velocity of aggregating cells	12μm/min	(Loomis, 2012)
	$\tilde{v}$	Rescaled cell velocity ($D \to \infty$ limit; see Sup. Information)	hour^{-1}	Varied	--		
	N_0	Initial number of P-cells	# cells	Varied	--		
	η	Decay constant of the signal	min^{-1}	1.2	Parameter used for model fitting.		
	D	Signal diffusion coefficient	cm^2/s	Varied	cAMP diff. coeff. (2% agar) CMF diff. coeff. (water film)	4.4x10^{-6} cm^2/s 8x10^{-7} cm^2/s	(Dworkin & Keller, 1977; Song et al., 2006; Yuen & Gomer, 1994)
Resource competition model	μ	Decrease rate of survival probability	hour^{-1}	2x10^{-3}	Number of alive/moving loners versus time	2x10^{-3} hour^{-1}	Fitting from (Dubravcic, 2013)
	ς	Resistance to starvation parameter	--	2		2	
	T_{sur}	Loner maximum lifespan	hour	240		240 hour	
	T_{ger}	Spore germination time	hour	4	Mean germination time 1-3 days old spores	4-8 hour	(Cotter & Raper, 1968)
	δ	Spore death rate	hour^{-1}	2x10^{-4}	--		
	c	Maximum division rate	hour^{-1}	0.173	Doubling time	4 hour	(Fey et al., 2007)
	s	Spore:stalk ratio	--	0.8	Spore:stalk proportion	~ 80:20	(Stenhouse & Williams, 1977)
	ω	Spore germination success	--	0.63	Germination efficiency	0.63	(Dubravcic et al., 2014)
	R_0, X_0	Food pulse size; normalized initial population size	# cells	3x10^5	--		
	$R_{1/2}$	Resources consumption half saturation constant	--	0.1R_0	--		
	$\bar{T}_{st}$	Mean starvation time	hour	Varied	--		

Table S1. Parameterization of the two theoretical models. CMF is conditioned medium factor.

Supplementary Information for

"Eco-evolutionary significance of loners"

F.W Rossine§, R. Martinez-Garcia§, A.E. Sgro, T. Gregor* & C.E. Tarnita*

Contents

1   Calculation of stationary signal profile

We assume that cells are punctual sources that release signal at a constant strain-specific rate γ. The signal has a spontaneous decay rate η and a diffusion coefficient D. Given these conditions, the equation that governs the spatiotemporal evolution of signal density, $\sigma(x, y; t)$, is

$$\frac{\partial \sigma(x, y; t)}{\partial t} = D\nabla\sigma(x, y; t) - \eta\sigma(x, y; t), \tag{1.1}$$

The first term on the right side of Eq. (1.1) accounts for the diffusion of signal and the second term for its spontaneous decay. Here, we first solve the stationary limit ($\partial_t = 0$) of Eq. (1.1) in an infinite domain, imposing as boundary conditions the facts that cells continuously release signals and that signal density goes to zero when the distance from the emitting cell tends to infinity. Subsequently, we discuss the effect of considering a finite integration domain with periodic boundary conditions.

Due to the radial symmetry of the problem, we transform Eq. (1.1) to polar coordinates, in which the partial differential equation in (x, y) becomes an ordinary differential equation in the radial coordinate r that indicates the distance to the source of the signal,

$$D\left(\frac{d^2\sigma(r)}{dr^2} + \frac{1}{r}\frac{d\sigma(r)}{dr}\right) - \eta\sigma(r) = 0. \tag{1.2}$$

Since the position of the emitter, $r = 0$, is a singular point of Eq. (1.2), we will first assume that cells have a finite radius $\tilde{r}$ and then take the limit $\tilde{r} \to 0$. After the transformation to polar coordinates, and assuming a finite radius for the cell, the boundary conditions can be written as,

$$\sigma_{\tilde{r}}(r \to \infty) = 0, \tag{1.3}$$

$$-2\pi\tilde{r}D\frac{d\sigma_{\tilde{r}}(r)}{dr}\bigg|_{r=\tilde{r}} = \gamma. \tag{1.4}$$

Eq. (1.3) imposes the finiteness of the density, and Eq. (1.4) imposes that the amount of mass released through the boundary of the cell per unit cell has to be constant and equal to the strain-specific emission rate γ. The subscript $\tilde{r}$ in the densities accounts for the finite radius of the cells.

Equation (1.2) is the modified Bessel equation of order zero, and its general solution can be expressed as

$$\sigma_{\tilde{r}}(r) = A I_0 \left(\sqrt{\frac{\eta}{D}} r \right) + B K_0 \left(\sqrt{\frac{\eta}{D}} r \right), \tag{1.5}$$

where I_0 and K_0 are the zero order modified Bessel functions of the first, respectively second, kind. From the boundary condition of Eq. (1.3), it follows that $A = 0$, since I_0 diverges when its argument tends to infinity. B is calculated from the second boundary condition, Eq. (1.4),

$$B = \frac{\gamma}{2\pi \tilde{r} \sqrt{\eta D} K_1 \left(\sqrt{\frac{\eta}{D}} \tilde{r} \right)}, \tag{1.6}$$

where K_1 is the first order modified Bessel function of the second kind and we have used that $K_0'(r) = -K_1(r)$.

Inserting Eq. (1.6) into (1.5), the stationary signal profile produced by a source of finite radius $\tilde{r}$ is,

$$\sigma_{\tilde{r}}(r) = \frac{\gamma}{2\pi \tilde{r} \sqrt{\eta D} K_1 \left(\sqrt{\frac{\eta}{D}} \tilde{r} \right)} K_0 \left(\sqrt{\frac{\eta}{D}} r \right). \tag{1.7}$$

Finally, to obtain the profile generated by a punctual source, we take the limit $\tilde{r} \to 0$ in Eq. (1.7),

$$\sigma(r) = \frac{\gamma}{2\pi D} K_0 \left(\sqrt{\frac{\eta}{D}} r \right). \tag{1.8}$$

The solution provided by Eq. (1.8) assumes an infinite system size, whereas we perform numerical simulations of the developmental model on a finite domain of lateral length ℓ with periodic boundary conditions. To impose periodic boundary conditions is equivalent to considering that the simulated finite domain corresponds to a tile embedded into an infinite lattice in which each tile is a mirroring image of the focal domain. The signal density within the focal tile is obtained by adding over the contributions of all other tiles. However, since our numerical simulations only explore a range of diffusion coefficients in which $\sigma(\ell/2) \approx 0$, we can truncate the sum over tiles at the nearest neighbors of the focal one. This is equivalent to calculating distances to the position of each emitting cell, $(x_{\text{em}}, y_{\text{em}})$, in each spatial coordinate:

$$r_x = \begin{cases} |x - x_{\text{em}}| & \text{if } |x - x_{\text{em}}| \leq \ell/2 \\ \ell - |x - x_{\text{em}}| & \text{if } |x - x_{\text{em}}| > \ell/2 \end{cases}$$

$$r_y = \begin{cases} |y - y_{\text{em}}| & \text{if } |y - y_{\text{em}}| \leq \ell/2 \\ \ell - |y - y_{\text{em}}| & \text{if } |y - y_{\text{em}}| > \ell/2 \end{cases}$$

The total distance is then given by the radial coordinate r, as $r = \sqrt{r_x^2 + r_y^2}$.

2 Analytical treatment of the developmental model in the spatially-implicit limit $D \to \infty$

The spatially-implicit limit of the individual based population-partitioning model consists of disregarding the spatial effects introduced by a finite signal diffusion coefficient (i.e. the limit $D \to \infty$), but still accounting for cell movement at a finite velocity. To this end, we map cell movement into a stochastic transition in cell

2

state from aggregating to being multicellular: the rate of this transition is related to cell velocity v.

First, we calculate the stationary signal density σ^{H} produced by each cell in the limit $D \to \infty$. Unlike in the low D case explored in the spatially-explicit simulations, in which periodic boundary conditions were implemented considering only the nearest neighbors of the focal tile, now, since the signal spreads infinitely far, we need to include the contribution of an infinite number of tiles. This results in each cell generating a homogeneous signal distribution within the focal tile, $\sigma^{\mathrm{H}} = \mathcal{M}/\ell^2$. $\mathcal{M}$ is the mass of signal that is being released by each cell in the stationary limit, which can be obtained by integrating Eq. (1.8) over the entire range of distances,

$$\mathcal{M} = \int_0^\infty r\sigma(r)dr = \frac{\gamma}{2\pi\eta}. \tag{2.1}$$

Due to the conservation of the total population size N_0 (since demographic events are neglected on the temporal scales of aggregation), the state of the system is fully determined by the sizes of two of the three subpopulations ($P, A,$ and M cells). We choose the number of cells in the P-state, N_P, and in the A-state, N_A, as state variables. The number of cells in the M state, $N_M(t)$ (i.e., the size of the multicellular aggregate) can then be obtained from $N_P(t) + N_A(t) + N_M(t) = N_0$.

In order for the aggregation process to be initiated at all, a quorum must be met by the initial population (all of which are P-cells), i.e. we must have $N_0\sigma^{\mathrm{H}} > \theta$. In the absence of a quorum, all initial cells remain as loners and therefore the total loner number is $L = N_0$. If there is an initial quorum, then P-cells turn into A-cells at rate λ; A-cells continue to emit signal while they move in the direction of the aggregate. As A-cells eventually join the aggregate, they stop signaling and therefore the amount of signal in the system continues to decrease. P-cells continue to become A-cells at rate λ only if the total signal density $[N_P(t) + N_A(t)]\sigma^{\mathrm{H}}$ remains above the strain-specific sensitivity threshold, θ. The P-to-A transition rate as a function of time is thus given by

$$\hat{\lambda}(t) = \lambda\Theta\left(\sigma^{\mathrm{H}}\left[N_P(t) + N_A(t)\right] - \theta\right), \tag{2.2}$$

where Θ is the Heaviside function, which takes value 1 for non-negative arguments and 0 for negative arguments. Therefore, omitting the temporal dependence in $\hat{\lambda}$, N_A and N_P,

$$\hat{\lambda} = \begin{cases} \lambda & \text{if } N_P + N_A \geq \theta/\sigma^{\mathrm{H}} \\ 0 & \text{otherwise.} \end{cases} \tag{2.3}$$

The rate at which A-cells stick to the aggregate and become M-cells can be approximated by the inverse of the time needed to cover the mean distance to the aggregate at a velocity v, i.e.

$$\tilde{v} = \frac{v}{<d>} \tag{2.4}$$

where $<d>$ is a characteristic spatial scale of the aggregation territory (mean distance to the aggregation center). For simplicity, we will fix $<d> = 1$ in the following and refer to $\tilde{v}$ as a rescaled velocity.

Therefore, the aggregation process can be mapped to a sequence of two stochastic reactions, each of which occurs at a different rate,

$$P \xrightarrow{\hat{\lambda}(t)} A \qquad\qquad A \xrightarrow{\tilde{v}} M, \tag{2.5}$$
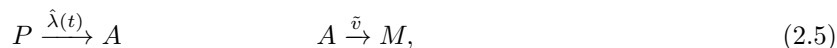
This stochastic process is fully described by a master equation, which gives the temporal evolution of the probability $g(N_P, N_A; t)$ of finding the system in a state (N_P, N_A) at time t,

$$\frac{\partial g(N_P, N_A; t)}{\partial t} = \tilde{v}(N_A + 1)g(N_P, N_A + 1; t) + \hat{\lambda}(N_P + 1)g(N_P + 1, N_A - 1; t) \tag{2.6}$$

$$- \left(N_P\hat{\lambda} + N_A\tilde{v}\right)g(N_P, N_A; t) \tag{2.7}$$

3

To simplify the notation, the temporal dependence in N_P, N_A and $\hat{\lambda}$ has been omitted.

Following standard procedures, from the master equation (2.7), we can derive a system of coupled ordinary differential equations for the mean value of each subpopulation size,

$$\dot{p}(t) = -\hat{\lambda}p(t) \tag{2.8}$$

$$\dot{a}(t) = \hat{\lambda}p(t) - \tilde{v}a(t) \tag{2.9}$$

where $p(t)$ and $a(t)$ are the mean values of N_P, respectively N_A, at time t. The dot over a and p on the left side of the equation indicates a time derivative. System (2.8) can be solved analytically, using that initially all cells are in the pre-aggregation state, i.e. $p(0) = N_0$, $a(0) = 0$. Then

$$p(t) = N_0 e^{-\hat{\lambda}t} \tag{2.10}$$

$$a(t) = \frac{\hat{\lambda}N_0}{\tilde{v} - \hat{\lambda}}\left(e^{-\hat{\lambda}t} - e^{-\tilde{v}t}\right). \tag{2.11}$$

Since the ultimate objective of this approximation is to obtain analytical expressions for the loner-aggregator partitioning behavior, an important observable is the time τ at which the decaying signal density exactly equals the strain-specific sensitivity threshold. τ can thus be obtained by solving

$$\theta = \sigma^{\mathrm{H}}[p(\tau) + a(\tau)] = \frac{\sigma^{\mathrm{H}}N_0}{\tilde{v} - \lambda}\left(\tilde{v}e^{-\lambda\tau} - \lambda e^{-\tilde{v}\tau}\right), \tag{2.12}$$

where we have used the fact that $\hat{\lambda}(\tau) = \lambda$ according to Eq. (2.2). Since aggregating cells also contribute to the pool of signal, τ does not represent the aggregation time; after a time τ, any A-cell in the system will continue to move towards the aggregate at rate $\tilde{v}$ until $a(\tau + \Delta t) = 0$. However, importantly, τ gives the time at which the last $P - A$ transition occurs. Therefore, all cells that are still in the P-state at time τ will remain as loners and we can find the total number of loners as

$$L = \begin{cases} p(\tau) & \text{if} \quad N_0\sigma^{\mathrm{H}} > \theta \quad \text{(i.e. a quorum is met)} \\ N_0 & \text{otherwise} \end{cases} \tag{2.13}$$

Henceforth we will focus on the former case, when aggregation does get initiated.

In general, we can not solve for τ in Eq. (2.12) and therefore we can not determine the number of loners analytically. Below, we try to circumvent this problem by looking at a few special cases.

2.1 Analytical results for the non-spatial limit $\tilde{v} \to \infty$

In this limit, cells spend an infinitesimally short time in the A state and therefore $p(t) + a(t) \to N_0 e^{-\lambda/t}$. To obtain τ we

then solve $\sigma^{\mathrm{H}}N_0 e^{-\lambda/\tau} = \theta$, which gives $\tau = \ln\left(\frac{\sigma^{\mathrm{H}}N_0}{\theta}\right)/\lambda$. Then, from Eq. (2.13), the number of loners, when there is a quorum for aggregation, is

$$L = \exp(-\lambda/\tau) = \theta/\sigma^{\mathrm{H}}. \tag{2.14}$$

Therefore, in this limit, λ gives the time scale of the aggregation but it has no effect on the number of loners, which is equal to the sensing-to-signal ratio.

4

In the special case $\tilde{v} = 2\lambda$, using the change of variables $y = \exp(-\lambda\tau)$, (2.12) becomes a quadratic equation from which y and thus τ can be obtained,

$$y^2 - 2y + \frac{\theta}{N_0\sigma^{\mathrm{H}}} = 0. \tag{2.15}$$

Given the definition of y, Eq. (2.15) only has physical meaning in the domain $y \in (0, 1]$. Within that interval, if a quorum exists (i.e. $N_0 > \theta/\sigma^{\mathrm{H}}$), Eq. (2.15) has a single root, which determines the number of loners $p(\tau)$ according to Eq. (2.10) and the definition of y:

$$L = N_0 y = N_0 \left(1 - \sqrt{1 - \frac{\theta}{N_0\sigma^{\mathrm{H}}}}\right). \tag{2.16}$$

In the limit $N_0 \to \infty$, Eq. (2.16) tends to $\theta/(2\sigma^{\mathrm{H}})$, as predicted by Eq. (1) in the main text (also Eq. (2.23) below).

In the other special case, $\tilde{v} = \lambda/2$, Eq. (2.12) becomes again Eq. (2.15) using the change of variables $y = \exp(-\tilde{v}t)$. Thus, if there is a quorum for aggregation (i.e. $N_0 > \theta/\sigma^{\mathrm{H}}$) the number of loners is

$$L = N_0 y^2 = N_0 \left(1 - \sqrt{1 - \frac{\theta}{N_0\sigma^{\mathrm{H}}}}\right)^2, \tag{2.17}$$

which tends to 0 in the limit $N_0 \to \infty$, as predicted by the phase separation defined by Eq. (1) of the main text (also Eq. (2.23) below).

In general, the changes of variables introduced here, $y = \exp(-\lambda t)$ and $y = \exp(-\tilde{v}t)$, will turn Eq. (2.12) into a polynomial equation of degree n provided that $\tilde{v} = n\lambda$ or $\tilde{v} = \lambda/n$. If the root of such a polynomial within the interval $y \in (0, 1]$ can be obtained, then an expression for the number of loners as a function of the initial population N_0 is accessible. In Figure S4, we show the two cases obtained here (Eqs. (2.16) and (2.17)), as well as the non-spatial limit $\tilde{v} \to \infty$. In addition, we also show the $\tilde{v} = 4\lambda$ case, where the equivalent to Eq. (2.15) is a 4-th degree polynomial, whose root in the interval $y \in (0, 1]$ we obtained using *Mathematica 11.1*.

2.3 Analytical results in the large population limit $N_0 \to \infty$

In the limit of infinitely large initial population size, a quorum is always met. Therefore, from Eq. (2.13), the number of loners is

$$L = \lim_{N_0 \to \infty} p(\tau) = \lim_{N_0 \to \infty} N_0 \mathrm{e}^{-\lambda\tau}. \tag{2.18}$$

At the end of this section, we prove that p is a positive and monotonically decreasing function of N_0; therefore L always exists and is greater than or equal to zero. This also implies that $\lim_{N_0 \to \infty} \mathrm{e}^{-\lambda\tau} = 0$ (otherwise L would not be finite); applying L'Hôpital's rule to Eq. (2.18), we obtain

$$L = \frac{N_0^2 \tilde{v}\sigma^{\mathrm{H}} \left[\mathrm{e}^{-2\lambda\tau} - \mathrm{e}^{-\lambda\tau}\mathrm{e}^{-\tilde{v}\tau}\right]}{\theta(\tilde{v} - \lambda)}, \tag{2.19}$$

where we have used Eq. (2.26) for the derivative of τ with respect to N_0. Finally, defining $Q \equiv \lim_{N_0 \to \infty} N_0 \mathrm{e}^{-\tilde{v}\tau}$ and rearranging terms, we get

$$L = Q + \frac{\theta(\tilde{v} - \lambda)}{\sigma^{\mathrm{H}}\tilde{v}}. \tag{2.20}$$

To obtain an independent expression for L we need another, non-redundant relationship between L and

5

Q. This can be obtained by first rearranging terms in Eq. (2.12)

$$N_0 \left[\frac{e^{-\lambda\tau}}{\lambda} - \frac{e^{-\tilde{v}\tau}}{\tilde{v}} \right] = \frac{(\tilde{v} - \lambda)\theta}{\tilde{v}\lambda\sigma^{\mathrm{H}}}, \tag{2.21}$$

and then taking the limit $N_0 \to \infty$ in Eq. (2.21),

$$\frac{L}{\lambda} - \frac{Q}{\tilde{v}} = \frac{(\tilde{v} - \lambda)\theta}{\tilde{v}\lambda\sigma^{\mathrm{H}}}. \tag{2.22}$$

Solving for L in Eqs. (2.19) and (2.22), we find

$$L = \begin{cases} 2\pi\eta\ell^2 \, \frac{\theta}{\gamma} \left(1 - \frac{\lambda}{\tilde{v}}\right) & \text{if } \lambda \le \tilde{v} \\ 0 & \text{if } \lambda > \tilde{v}, \end{cases} \tag{2.23}$$

where we have used the fact that $\sigma^{\mathrm{H}} = \frac{\gamma}{2\pi\eta\ell^2}$ (see Section 2). In the limit $N_0 \to \infty$, there is thus a phase separation given by the relative magnitudes of the P-to-A and A-to-M transition rates.

Proof of the existence of L. In order to obtain in Eq. 2.23 the limit of $p(\tau)$ for infinite initial population sizes, we first need to prove that such a limit exists and is finite. To this end, we will first calculate the derivative of $p(\tau)$ with respect to N_0:

$$\frac{dp(\tau)}{dN_0} = e^{-\lambda\tau} - N_0\lambda\tau'(N_0)e^{-\lambda\tau}, \tag{2.24}$$

Although Eq. (2.12) for τ cannot be solved in general, we can obtain an analytical expression for the derivative of τ with respect to N_0 using implicit differentiation. We differentiate both sides of Eq. (2.12)

$$\left[\tilde{v}e^{-\lambda\tau} - \lambda e^{-\tilde{v}\tau}\right] + N_0 \left[-\lambda\tilde{v}\tau'(N_0)e^{-\lambda\tau} + \tilde{v}\lambda\tau'(N_0)e^{-\tilde{v}\tau}\right] = 0, \tag{2.25}$$

and solving for $\tau'(N_0)$, we obtain

$$\tau'(N_0) = \frac{1}{\tilde{v}\lambda N_0} \left[\frac{\tilde{v}e^{-\lambda\tau} - \lambda e^{-\tilde{v}\tau}}{e^{-\lambda\tau} - e^{-\tilde{v}\tau}}\right], \tag{2.26}$$

which is always positive for any relationship between $\tilde{v}$ and λ. Using Eq. (2.26) in Eq. (2.24), we find

$$\frac{dp(\tau)}{dN_0} = e^{-\lambda\tau} \left[1 - \frac{e^{-\lambda\tau} - \frac{\lambda}{\tilde{v}}e^{-\tilde{v}\tau}}{e^{-\lambda\tau} - e^{-\tilde{v}\tau}}\right] = \frac{e^{-(\lambda+\tilde{v})\tau}\left(\frac{\lambda}{\tilde{v}} - 1\right)}{e^{-\lambda\tau} - e^{-\tilde{v}\tau}} \tag{2.27}$$

Since the numerator and the denominator of Eq. (2.27) have opposite signs for both $\lambda > \tilde{v}$ and $\tilde{v} > \lambda$, $dp(\tau)/dN_0$ is always negative. Thus, $p(\tau)$ is a decreasing function of N_0. Since p is a non-negative and decreasing function, the limit of $p(\tau)$ as N_0 tends to infinity exists and is always greater than or equal to zero. Importantly, due to the symmetry between p and $N_0 \exp(-\tilde{v}\tau)$, the limit Q defined in the calculation of L also exists and has the same properties as L.

2.4 Analytical results for co-development of two strains with same λ and $\tilde{v} = 2\lambda$

In mixed development, we consider two strains defined by the set of strain-specific parameters $(\lambda, \theta, \gamma)$. λ and θ have been defined above, and γ determines the strain-specific signal density σ^{H} released by each cell. We use the term *high-threshold strain* and the notation ht for the strain with the higher signal sensitivity threshold and *low-threshold strain* (lt) for the one with the lower signal-sensitivity threshold. Thus, $\theta_{ht} > \theta_{lt}$.

6

If both strains have the same strain-specific λ, which is the case studied in this section, then the high-threshold strain also has the higher investment (i.e., it is the worse aggregator) if

$$\frac{\theta_{ht}}{\sigma_{ht}^{\text{H}}} > \frac{\theta_{lt}}{\sigma_{lt}^{\text{H}}}. \tag{2.28}$$

To obtain the mixed loners, we generalize Eq. (2.12) to the two-strain case,

$$\sigma_{ht}^{\text{H}}[p_{ht}(\tau_{ht}) + a_{ht}(\tau_{ht})] + \sigma_{lt}^{\text{H}}[p_{lt}(\tau_{lt}) + a_{lt}(\tau_{lt})] = \theta_{ht}, \tag{2.29}$$

where τ_{ht} is the time at which the density of signals reaches the strain-specific sensitivity of the high-threshold strain. Therefore, for $t > \tau_{ht}$, $\hat{\lambda}_{ht} = 0$ and only cells of the low-threshold strain continue to aggregate ($\hat{\lambda}_{lt} \neq 0$).

Let Π be the proportion of the high-threshold strain in the mix; ΠN_0 is thus the initial population of the high-threshold strain, and $(1 - \Pi)N_0$ the initial population of the low-threshold strain. Substituting the expressions for $a(t)$ and $p(t)$ obtained in Eqs. (2.10) and (2.11), Eq. (2.29) becomes

$$\frac{N_0 \Pi \sigma_{ht}^{\text{H}}}{\tilde{v} - \lambda_{ht}} \left[\tilde{v} \mathrm{e}^{-\lambda_{ht}\tau_{ht}} - \lambda_{ht}\mathrm{e}^{-\tilde{v}\tau_{ht}} \right] + \frac{N_0(1 - \Pi)\sigma_{lt}^{\text{H}}}{\tilde{v} - \lambda_{lt}} \left[\tilde{v}\mathrm{e}^{-\lambda_{lt}\tau_{ht}} - \lambda_{lt}\mathrm{e}^{-\tilde{v}\tau_{ht}} \right] = \theta_{ht}. \tag{2.30}$$

τ_{ht} cannot be obtained from Eq. (2.30) in general. However, since we assume in this section that $\lambda_{ht} = \lambda_{lt} \equiv \lambda$ and $\tilde{v} = 2\lambda$, then the change of variables $y = \exp(-\lambda\tau_{ht})$ turns Eq. (2.30) into a quadratic equation of the form

$$y^2 - 2y + \frac{\theta_{ht}}{N_0\Pi(\sigma_{ht}^{\text{H}} - \sigma_{lt}^{\text{H}}) + N_0\sigma_{lt}^{\text{H}}} = 0, \tag{2.31}$$

that has only one root in the interval $(0, 1]$. Using that root, we obtain the number of loners of the high-threshold strain,

$$L_{ht} = \Pi N_0 y = \Pi N_0 \left(1 - \sqrt{1 - \frac{\theta_{ht}}{N_0\Pi(\sigma_{ht}^{\text{H}} - \sigma_{lt}^{\text{H}}) + N_0\sigma_{lt}^{\text{H}}}} \right) \tag{2.32}$$

After τ_{ht}, only cells of the low-threshold strain continue to aggregate. The number of loners left by the low-threshold strain is determined by the relationship between L_{ht}, σ_{ht}^{H}, and θ_{lt}:

- If $\sigma_{ht}^{\text{H}}L_{ht} \geq \theta_{lt}$ the loners of the high-threshold strain provide quorum for a full aggregation of the low-threshold strain and therefore $L_{lt} = 0$.

- If $\sigma_{ht}^{\text{H}}L_{ht} < \theta_{lt}$, the low-threshold strain stops aggregating at a time $\tau_{lt} > \tau_{ht}$, such that

$$\sigma_{ht}^{\text{H}}L_{ht} + \sigma_{lt}^{\text{H}}p_{lt}(\tau_{lt}) = \theta_{lt}, \tag{2.33}$$

which gives the number of loners for the low-threshold strain

$$p_{lt}(\tau_{lt}) \equiv L_{lt} = \frac{\theta_{lt}}{\sigma_{lt}^{\text{H}}} - \frac{\sigma_{ht}^{\text{H}}\Pi N_0}{\sigma_{lt}^{\text{H}}} \left(1 - \sqrt{1 - \frac{\theta_{ht}}{N_0\Pi(\sigma_{ht}^{\text{H}} - \sigma_{lt}^{\text{H}}) + N_0\sigma_{lt}^{\text{H}}}} \right) \tag{2.34}$$

The transition from one outcome to the other occurs at a population composition $\tilde{\Pi}$ such that $\sigma_{ht}^{\text{H}}L_{ht} = \theta_{lt}$. Using Eq. (2.32) for the number of loners of the high-threshold strain, we obtain

$$\tilde{\Pi} = \frac{2\theta_{lt}\sigma_{lt}^{\text{H}}}{\sigma_{ht}^{\text{H}}(\theta_{ht} - 2\theta_{lt}) + 2\theta_{lt}\sigma_{lt}^{\text{H}}}. \tag{2.35}$$

7